2007

# Nanoripples formation in calcite and indium phosphide (InP) single crystals

Ramakrishna Gunda
*University of South Florida*

# Nanoripples Formation in Calcite and Indium Phosphide (InP) Single Crystals

by

Ramakrishna Gunda

A thesis submitted in partial fulfillment
of the requirements for the degree of
Master of Science in Mechanical Engineering
Department of Mechanical Engineering
College of Engineering
University of South Florida

Major Professor: Alex A. Volinsky, Ph.D.
Ashok Kumar, Ph.D.
Nathan B. Crane, Ph.D.

Date of Approval:
November 8, 2007

Keywords: Calcite, InP, Nanowear ripples, Ion Beam Irradiation, Nanoindentation

Acknowledgements

I would like to express my heartfelt gratitude to my advisor Prof. Alex A. Volinsky for his guidance, suggestions and constant encouragement. It was great pleasure to conduct this work under his supervision. I sincerely thank my lab members Jayadeep Deva Reddy, Patrick Waters, Megan Pendergast, Xiolu Pang for their help in various ways. I am thankful to Prof. Marek Szymonski, Dr. F. Krok, Dr. Janusz Budzioch, Dr. Om Prakash Sinha and Salah R. Saeed for providing unique opportunity to conduct research in Jagiellonian University, Krakow Poland. I would like to thank National Science Foundation (CMMI-0631526), the Division of Design, Manufacture and Industrial Innovation, and the IREE Supplement, as well as Hysitron Inc., for support.

Table of Contents

List of Figures

Nanoripples Formation in Calcite and Indium Phosphide (InP) Single Crystals

Ramakrishna Gunda

ABSTRACT

In this project we studied the formation of nanoripples in calcite and InP single crystals by continuous scanning using the nanoindenter in the ambient environment and by $Ar^+$ irradiation under ultra high vacuum (UHV) conditions, respectively.

Formation of tip-induced nanowear ripples is studied on a freshly cleaved calcite single crystal as a function of scanning frequency (1 - 3 Hz) and contact load (2 - 8 μN) of the diamond tip. At lower loads (≤ 4 μN), initiation of the ripples takes place at the bottom of the surface slope at 3 Hz scanning frequency, which continue to propagate as scanning progresses. The orientation of these ripple structures is perpendicular to the scan direction. As the number of scans increases, ripples fully develop, and their height and periodicity increase with the number of scans by merging ripples together. At 6 μN normal load, tip-induced wear occurred as the tip started removing the ripple structures with increased number of scan cycles. As the contact load increased further, a ripple structure was not initiated and only tip-induced wear occurred on the surface. At 1 Hz frequency material removal takes place as the tip moves back and forth and material slides towards the scan edges. Material removal rate increased with contact load and it is observed that the number of scans required to create a new surface is inversely proportional to the contact load. Possible mechanisms responsible for the formation of ripples at higher frequencies are attributed to the slope of the surface, piezo hysteresis,

system dynamics or a combination of effects. Single crystal calcite hardness of 2.8 GPa and elastic modulus of 80 GPa were measured using nanoindentation.

Evolution of nanostructures on the InP (100) surface due to ion bombardment has been studied with scanning tunneling microscopy in UHV environment. InP (100) crystal surfaces were irradiated by $Ar^+$ ion incident beam with 3 KeV energy at an incident angle of $75^o$. Self-organization of the surface was studied by varying the ion fluence from 7.7 $x10^{13}$ to 4.6 $x10^{17}$ ions/$cm^2$. The observed nanoripple morphologies have been explained based on the concept of interplay between roughening and smoothing processes. Wavelength of the nanostructures linearly increases with the logarithm of the fluence ($\varphi$). The rms roughness is approximately linear with the logarithm of the fluence. Nanoindentation experiments were performed on InP surface before and after ion bombardment to determine variation in hardness (H) and elastic modulus (E). Surface of irradiated InP has higher H and E values as the surface become amorphized after $Ar^+$ ion bombardment.

# Chapter 1

# Introduction and Literature Review

## 1.1 Introduction

The development of the field of nano-mechanics of materials and coatings over the past few decades gave a significant amount of contact mechanical methods for determination of mechanical and tribological properties of materials at micro and nano scales. Among others, nanoindentation and micro/nanotribology methods have been considerably developed, including depth sensing nanoindentation and Atomic Force Microscopy (AFM)/Scanning Tunneling Microscopy (STM). These are powerful and versatile tools for characterization of surface topographies and for investigating local mechanical properties at small scales. In addition, it has been made possible to take advantage of the scanning capability of the nanoindenter to scan the surfaces continuously to modify the materials structure.

As the use of coatings constantly increases in the field of nanotechnology, it is important to know the behavior of materials at small scales. In recent years, the formation and characterization of nanometer-sized structures have attracted a great deal of interest. One of the motivations of nanotechnology research is the construction of nanosized surface patterns. In a typical wear experiment a hard material is scanned over the tested material surface, resulting in a wear rate measurement in terms of the removed material depth as a function of normal applied load and number of wear cycles. When applying moderate forces in combination with repeated scanning over the same region, one could

observe a periodic ridged pattern, called wear ripples, oriented perpendicular to the direction of motion of the tip. Well-known examples are given by wind-blown sand dunes observed in deserts and on the sea shore [1]. Self-organization of surface undulations has also been reported at nanometer scale. For example, ripples are formed when glasses, amorphous films, semiconductors, or other metals are sputtered by ion beams [2]. These features have typical wavelengths of few tens of nanometers, and can be imaged by scanning probe microscopy. Leung and Goh observed the formation of ripples when the tip of an atomic force microscope (AFM) was scanned over a polymer film [3]. The orientation of the ripples was perpendicular to the scan direction and their characteristic wavelength was in the range between 10 and 100 nm. Ripples produced by scratching were observed on polymers several times, and, more recently, even on gold films [4]. The ripples were considered to be the result of a peeling process operated by the microscope tip in the case of polymer films [5], or as a result of a self-regulating periodic pickup and release of clusters in the case of gold films [4]. These patterns have also been seen in a wide variety of amorphous and semi-crystalline polymer systems.

The main interest for the development of nanopatterned surfaces is their potential application, such as templates for growing nanowires and nanorods, buffer layers for the growth of good crystalline epilayers, and strain relaxed heteroepitaxial films. Conventional patterning by electron beam lithography can yield regular nanostructures, but it is costly and gives a low throughput for large scale fabrication. Therefore, nanostructures synthesized on the basis of self-organization phenomena induced by ion bombardment offer an attractive solution because of its compatibility and reproducibility with easily controllable fabrication conditions and a cost efficient bottom up approach.

Since the ion sputtering is atomic by its nature, some characteristic dimensions of the surface structures could easily be on the order of nanometers. However, the approach of nanostructuring by self-organization often has the disadvantage of less control of structure, size, shape and ordering of the nanostructures compared to lithographic techniques.

Several papers in the recent literature report on the formation of ripple structures by the erosion of materials by ion sputtering. These structures are formed in different materials by the incidence of the ions at normal angles to the surface of the material. This is seen very clearly in Si and the propagation of surface ripples during Ga ion beam erosion of Si was measured in real time by combining focused ion beam technology with scanning electron microscopy [6].

## 1.2 Literature review

### 1.2.1 Nanostructuring of materials by various techniques

Nanopatterning or structuring of the materials can be produced by three different methods, which include:

1. Formation of tip-induced wear ripples by repeated scanning over the surface of the material using scanning probe microscope i.e. Atomic Force Microscope, and by using scanning capability of depth sensing nanoindenter
2. Nanostructuring of surfaces by ion beam irradiation
3. Erosion ripple formation by impact with abrasive particles

### 1.2.2 Formation of nanoripples by repeated scanning

Tip-induced nanopatterns or nanowear ripples on a surface of materials can be produced by scanning it repeatedly for a number of cycles and applying moderate normal forces using atomic force microscope or scanning Triboindenter. Although the main function of the atomic force microscope is imaging the surfaces at the nanoscale, it can also scan them continuously and modify their structure. Triboindenter is mainly used for measuring hardness and elastic modulus at the nanoscale, while by using the scanning feature of the Triboindenter, one can produce nanowear ripples or nanostructures on the materials surface.

Initially tip-induced wear patterns were observed in InSb crystals using atomic force microscope in the ultra high vaccum environment [7]. Few tens of nanonewtons of normal load were applied to scan repeatedly over the 1x1 $\mu m^2$ InSb (100) surface, which resulted in a creation of ripples perpendicular to the scan direction. Tip-induced surface patterning was explored on various materials including semiconductor surfaces [8-11]. Atomic size features such as stick-slip phenomenon in atomic force friction images had been recognized for quite a long time [12], but a deeper insight of the tip-induced wear and crystal surface modification was gained only recently [13-15]. The complete understanding of the process is still far from being established. An AFM tip moving over the surfaces induces material displacement. Few groups showed that prolonged scratching of the different material surfaces, such as polymers [16-19], ionic crystals and metals in the ultra high vaccum environment [14] and adsorbed gold particles on the polymer surface [20] resulted in formation of periodic ripples. Understanding this process at the nanoscale is crucial from the standpoint of future devices functionality, including

micro electro mechanical systems (MEMS). This process seems to be universal for various materials, as similar structures are observed in nature at different scales, including ripple patterns that cover sand dunes, rail tracks and clouds.

Similar work has been done on KBr and Al single crystals [21] in the ambient environment using nanoindenter. Ripples were observed on KBr after 20 scan cycles at 3 Hz scan frequency over a 5 x 5 $\mu m^2$ surface area with 2 μN normal force. The height of the ripples was 100 nm, and they were spaced 1 μm apart. Tip-induced wear ripples were also reproduced on gold samples in the presence of water using the Triboindenter [22]. Ripple patterns were not observed when repeated scanning was performed in the ambient environment with atomic force microscope. In this work, we made an effort to create nanowear ripples on the surface of calcite single crystals using a diamond tip of the Hysitron Triboindenter in the ambient environment. These results are presented in Chapter 3.

### 1.2.3 Nanopatterning or structuring by ion beam irradiation

Ion irradiation of a solid surface can be used to control surface morphology at a length scale ranging from 1 micron down to 1 nanometer. Focused or unfocused ion-beam irradiation induces spontaneous self-organization of the surface into nanometer-sized ripples, dots, or holes; it also induces diameter increase or decrease in pre-existing nanopores. Ion bombardment of surfaces is an integral part of many surface processing techniques, including ion sputter etching and deposition, sputter cleaning, ion beam assisted deposition, and reactive ion beam etching. These processes often result in pronounced topography evolution, generally accomplished by kinetic roughening of the surface. Under off-normal ion- beam incidence, a periodic height modulation in the form

of ripples or wavelike structures with submicron wavelength develops during ion bombardment as observed in single crystalline semiconductor materials (Si [23–25]; Ge [26]; InSb [27]), single crystalline metals (Cu [28, 29]) and glasses. The controlled growth of these semiconductor nanostructures has attracted considerable attention for the development of future photonic and electronic devices and for possible use in nanotechnology applications. Recently, the formation of surface patterns by ion bombardment was utilized for growth of low-dimensional vertical nanostructure templates [30].

Off-normal ion bombardment leads to the formation of periodically modulated structures on the irradiated surfaces depending on ion energy, ion mass, ion fluence, incidence angle, temperature, and surface orientation. For the incidence angles between $30^{o}$ and $60^{o}$ to the surface normal, ripples were formed with the wave vector parallel to the ion flux projection onto the surface, while for larger incidence angles the wave vector rotated to be perpendicular to the ion flux projection [3]. Recently several studies [31, 32] revealed that low energy ion bombardment normal to the sample surface produced regular arrays of conical or pyramidal features. Facsko et al. have observed the formation of hexagonal symmetric nanostructures on crystalline or amorphous GaSb and InSb with low-energy $Ar^{+}$ ion irradiation under normal incidence [33, 34]. Frost et al. have observed high density and spatially ordered dot structures on InP surfaces by low-energy $Ar^{+}$ ion irradiation [35]. Gago et al. reported the formation of self-assembled crystalline silicon nanostructures of homogeneous 15 nm height, arranged in a hexagonal symmetry, by low energy $Ar^{+}$ ion irradiation at normal incidence on Si (100) surface [36]. Recently, Ziberi et al. reported highly ordered self-organized dot patterns on Si (100) surface by low

energy $Ar^+$ ion- beam erosion [37]. Several authors have also reported the formation of ripples on Si (100) surface by low-energy $Ar^+$ ion irradiation at off-normal incidence [38, 39]. Recently F. Krok et.al, found that ion bombardment of InSb at an oblique angle of incidence led to the formation of wire-like structures on the surface with a diameter of tens of nanometers [40, 41].

Many techniques for measuring surface morphology have been applied to the study of ion-induced pattern formation. Initial observations were performed using scanning electron microscopy (SEM) [42], but because of the poor depth contrast of SEM, only ripples with large amplitudes could be studied. Development of high-resolution techniques such as scanning tunneling microscopy (STM) and atomic force microscopy opened new horizons for wide investigation of the surface solid structures at the microscopic scale down to atomic resolution. In this case, the excellent depth sensitivity and spatial resolution of these techniques have made it possible to study the surface morphology and periodicity. One of the main problems facing this research is the production of features in a controllable and regular fashion. It would be highly beneficial to produce nanostructures in a controllable manner, if there was a successful guiding analytical theory describing bombardment-induced topography. Unfortunately, most theories are basically qualitative ones [43]. There are only few quantitative analytical theories [44], which usually have limited ranges of applicability. In order to test these theories and to improve their predictability, more experimental studies are needed.

### 1.2.4 Theory of nanopattern formation

All theories of sputter pattern formation originate from Sigmund's model [45], demonstrating the instability of a planar surface due to uniform ion beam erosion.

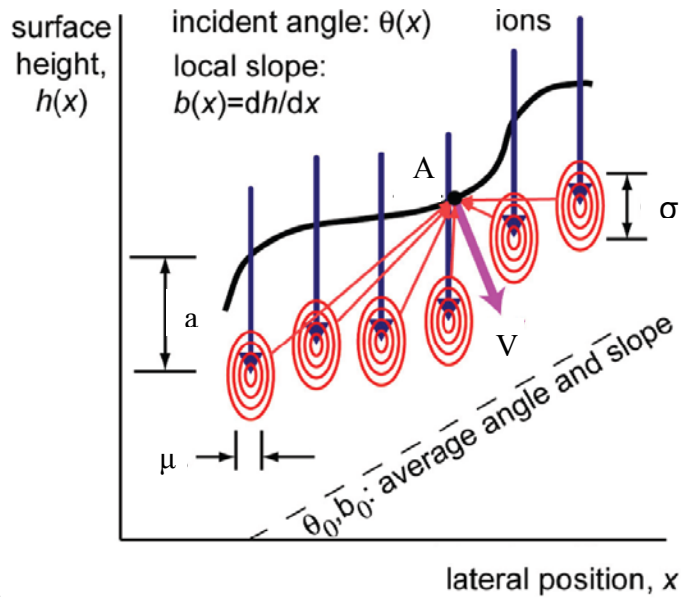


**Figure 1.1. Sigmund's (1973) model of sputter morphology evolution. Iso-energy contours are illustrated. Average ion range is *a*, longitudinal and transverse straggling are *σ* and *μ*. As illustrated by red arrows, some energy from ions impinging at all points contributes to erosion at point A. Concave regions such as *A* are closer to the energy deposition maxima than convex regions and thereby erode faster. [*From Nanoscale morphology control using ion beams by M.J. Aziz*].**

In Figure 1.1, ion beam approaches the solid in the *y*-direction and surface height is described by the function $y = h(x, t)$, where $t$ is time. The rate of recession of an eroding surface (excluding surface relaxation and noise) can be written as:

$$\frac{\partial h}{\partial t} = -V\sqrt{1+b^2} \qquad (1.1),$$

where $b \equiv \partial h/\partial x$ is the local slope of the surface and $V$ is the erosion speed normal to the surface. According to Sigmund, $V$ at point $A$ at position $x$ on the surface is proportional to the energy $E(x, x')$ deposited per unit depth at $x$ from the collision cascades originating from ions impinging on the surface at all other points $x'$, as shown in Figure 1.1. The speed of erosion at $x$ is then given by an integral over all points $x'$,

$$V(x) \propto \int E(x,x')dx' \tag{1.2}$$

As can be seen from Figure 1.1, concave regions of the surface, such as point $A$, are closer to the energy deposition maxima than convex regions, so they erode faster. For simplicity, Sigmund modeled the distribution of deposited energy as centered at a distance $a$ below the impingement site (along the initial ion direction) and decaying outward as a Gaussian with an ellipsoidal shape. $E(x, x')$ then becomes:

$$E(x,y,x',y') = (const.)\exp\left[-\left[\frac{[h(x')-a-h(x)]^2}{2\sigma^2}\right]-\frac{[x'-x]^2}{2\mu^2}\right] \tag{1.3}$$

Equation 1.1 was referred to as the *Sigmund sputter integral* and Equation 1.2 as the *Sigmund kernel*. Note that the only materials parameters controlling morphology evolution in this model are $a$, $\sigma$, and $\mu$. Parameters such as the surface binding energy merely scale with the rates for all points on the surface by a multiplicative factor through the proportionality constant in Equation 1.3.

### 1.2.5 Bradley and Harper instability theory

The most widely accepted model of the ripple formation is the linear Bradley-Harper model [3]. Starting from Sigmund's theory of sputtering [45], Bradley and Harper created a model, which explains why ion bombardment produces periodic height modulations on the surface of amorphous solids. The rate at which the material is sputtered from a point on a surface is proportional to the power dissipated there by the random distribution of the incoming ions. Ions penetrate the surface and transfer their kinetic energy to the atoms of the substrate, which may start secondary collisions, thereby generating other recoiling atoms. A small fraction of the atoms are sputtered away, while some of them are permanently removed from their sites, making the substrate locally amorphous. This theory is valid for small amplitudes only so that non-linear terms are neglected. The height of the surface is defined as $h(r, t)$ at any position, $r = (x, y)$, and time $t$. The evolution of the $h(r, t)$ is determined by a balance between roughening and smoothing processes that occur during sputtering, as shown schematically in Figure 1.2. The roughening is due to removal of atoms from the surface by sputtering while the smoothing is accomplished by surface diffusion or other surface transport.

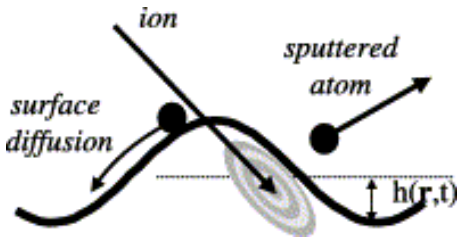


**Figure 1.2. Schematic representation of processes contributing to formation of ion-induced patterns.**

The elliptical contours around the ion path represent contours of constant energy deposition. The deposition of energy below the surface by the ion beam interacts with the surface morphology to preferentially remove atoms at the bottom of the trough of the surface wave. Surface diffusion reduces the surface curvature. The probability of sputtering at a particular point on the surface is proportional to the amount of energy deposited there, and it turns out that the local sputter yield is therefore proportional to the curvature of the surface:

$$\frac{\partial h}{\partial t} = S_x \frac{\partial^2 h}{\partial^2 x} + S_y \frac{\partial^2 h}{\partial^2 y} \tag{1.4}$$

The sputter roughening parameters, $S_x$ and $S_y$ are linearly proportional to the ion flux and depend in a complex way on the incidence angle and ion beam parameters. Surface diffusion balances the ion-induced roughening as described by Herring [46] and Mullins [47]. Diffusion driven by surface energy minimization occurs by smoothing the surface morphology and is proportional to the divergence of the surface curvature:

$$\frac{\partial h}{\partial t} = -B\nabla^4 \tag{1.5}$$

The constant of proportionality B, is given by

$$B = \frac{D_s C_{ss} \gamma}{n^2 kT} \tag{1.6},$$

where γ is the surface energy, $D_s$ is the diffusivity, $C_{ss}$ is the concentration of the mobile species on the surface, $n$ is the atomic density, $k$ is Boltzmann's constant and $T$ is the surface temperature in K.

### 1.2.6 Nanopatterning of surfaces by ion sputtering

In 1956 Navez et.al. [1] observed for the first time a curious phenomenon that bombardment of ions on a glass produced a new morphology depending mainly on the incidence angle $\theta$ of the ion beam. The results are reported in Figure 1.3. A clean glass surface has been exposed for 6 h to the ion beam at incidence angles ranging from 30° to 80°. The surface is covered by wavelike structures (ripples) separated by distances ranging from 30 ($\theta = 80°$) to 120 nm ($\theta = 30°$), which are stable under ambient conditions after the ion bombardment is finished. For incidence angles close to $\theta = 0°$ the ripples are perpendicular to the ion beam direction, while they rotate by 90° when the beam reaches the surface at grazing incidence angles. In contrast, when the bombardment is performed at normal incidence, one observes a structure formed by semi-spherical elements 40 nm in diameter.

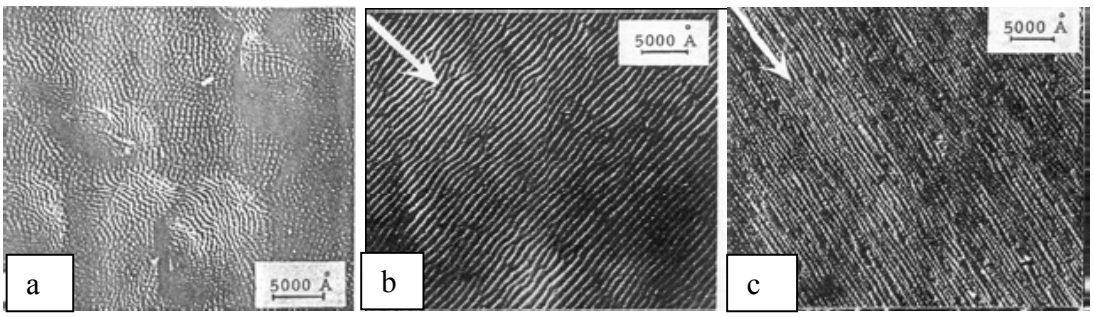


**Figure 1.3. Glass surface after 6 hrs bombardment. The arrow indicates the projection on the ion beam surface. The ripples align perpendicular to the ion beam. (a) $\theta = 30°$ (b) Same as (a) with $\theta = 0°$, (c) same as (a) with $\theta = 80°$. The ripples align along the ion beam direction.**

The authors did not provide an accurate explanation at that time, but simply tried to find analogies with macroscopic phenomena such as the ripple structures formed by wind over a sand bed. Figure 1.4 shows images of ripples observed in an Australian desert (Figure 1.4(a)), which are very similar to the features observed on the glass modified by ion bombardment in Figure 1.3. The formation of ripples on a sand dune occur because the sand particles are small and thus behave like a fluid. Air and sand can be considered as two immiscible fluids moving at very different speeds. When air and sand come into contact, the boundary between them can develop complex wavelike structures and ripples form along the boundary. The wind can pick up sand particles from the dune and move them around. If a small sand pile or a hollow forms somewhere, it will disrupt the airflow around it. The wind, forced to flow over or around the pile, slows down and can no longer carry as much sand with it, and it is therefore forced to deposit sand on the pile, which becomes larger and larger. The opposite occurs in the presence of a hollow. The wind increases its speed and sweeps more sand from the hollow. The entire process is unstable and the piles become larger and the hollows deeper. Eventually they form the ripples one can see on the dune.

The similarities are very close even in anomalies, for instance the change in orientation of an obstacle. The sand ripples (Figure 1.4(c)) align at the base of the dune as it occurs in glass, where in the presence of an impurity ripples align parallel to the existing defect (Figure 1.4(b)).

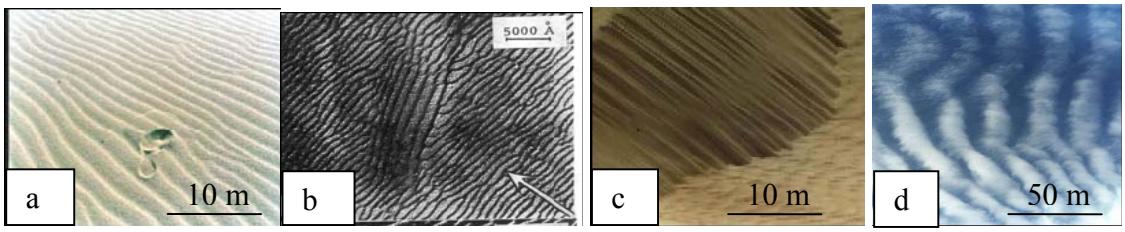


**Figure 1.4. Comparison of ripples in nature with ripples on glass surface. (a) Sand ripples on a dune in an Australian desert. (b) Glass surface after 6 h bombardment, $\theta$ = 45°. The arrow indicates the projection on the surface of the ion beam. (c) Sand ripples on a dune in a desert (Algeria). The ripples on the dune have different orientation with respect to the ripples in the open desert. (d) The clouds are the tops of the ripples between the dry, cool air above and the moist, warm air below**.

There are many other phenomena that produce similar patterns; for example strong similarities can be found in cumulus clouds on a partially sunny day. Figure 1.4(d) shows a picture of clouds: in this case the clouds are the tops of the ripples between the dry, cool air above and the moist, warm air below. The ion bombardment of a solid surface also looks very similar to the phenomenon of the sandblasting of solid surfaces [48], a method widely used for finishing metallic surfaces. When a solid surface is eroded by a stream of abrasive particles a regular ripple pattern is created perpendicular to the surface component of the incident stream with a wavelength comparable to the distance over which a single particle is in contact with the surface. This phenomenon very closely resembles the ion bombardment, where the erosion is produced by the 'abrasive' mechanism of the ion impinging on the surface. Even if the results are only qualitatively similar, the use of ion erosion for forming patterned surfaces is often called *ion sandblasting*. Nowadays, when the formation of periodic nanostructures is the key issue in the emerging field of nanotechnology, the understanding of the basic mechanisms of the ion sandblasting will allow us to extend the use of such a technique to a large variety of fabrication processes, allowing the in-situ production of substrates with well defined

vertical roughness, lateral periodicity, controlled step size and orientation. The latter process can be defined as a sort of new lithography, which is based on the re-organization of atoms and vacancies induced by ion bombardment, thus potentially opening new frontiers in the technology of thin films.

### 1.2.7 Patterning of amorphous materials

The Bradley and Harper model was very successful in predicting the ripple wavelength and orientation. There are many experiments performed on amorphous materials, which show the morphology predicted by the model. Very similar considerations apply for the case of single-crystal semiconductor surfaces, which upon ion impact become amorphized in the surface layers and thus lose the relationship with the high-symmetry directions of the bulk. A review of the use of ion sputtering in semiconductors appeared recently [49]. Apart from the early experiments on glass previously reported in Figure 1.3, extensive work was carried out by several authors in the last decades [50, 51].

### 1.2.8 Patterning of metals

Particular attention should be devoted to the case of metals. Due to the higher diffusivity in semiconductors compared to amorphous materials and to the non-directional character of the metallic bond, the ion impact does not imply the amorphization of the surface, at least for low ion fluences. In the case of metals, the build-up of a regular pattern is produced by two different mechanisms, which lead to a similar surface instability: the surface curvature dependence of the ion sputtering and the presence of an extra energy barrier whenever diffusing adatoms try to descend step edges.

The effect was observed by Rusponi *et.al.* [52] on Ag (110) and later on Cu (110) [53, 54]. In conclusion, diffusive processes are mainly responsible for the formation of regular structures on metal surfaces under ion bombardment; however, the temperature hierarchy of these processes cannot explain all observations if another source of instability is not considered in the model.

## 1.3 Objectives

In this work, we made an effort to produce tip-induced nanowear ripples on calcite single crystals using Hysitron Triboindenter in the ambient environment conditions. Our objective was to replicate the nanowear ripples observed in the ultra high vaccum atomic force microscope (UHV-AFM) and to determine the mechanism responsible for the formation of these ripples. We also made an effort to study the nanopatterning of Indium Phosphide (InP) single crystal surfaces due to $Ar^+$ ion bombardment as a function of ion fluence in the ultra high vaccum environment.

This chapter reviewed the formation of tip-induced nanowear ripples and nanostructuring of substrates by ion bombardment and its importance in the field of nanotechnology. In both techniques surface modification takes place and needs to be studied. In order to evaluate the surface morphology, various surface imaging techniques were used. The following chapter covers various surface imaging techniques, which were used in our experimental work.

# Chapter 2

## Surface Imaging Techniques

### 2.1 Scanning probe microscopy

In scanning probe microscopy (SPM) images are formed by using a physical probe that scans the surface [55]. An image of the surface is obtained by mechanically moving the probe in a raster scan, line by line, and recording the probe-surface interaction as a function of position. SPM was founded with the invention of the scanning tunneling microscope (STM) in 1981. Since the invention of the STM, probe microscopies have made a broad impact in material science, semiconductor physics, biology, tribology, surface thermodynamics and micromechanics. SPM is unique among imaging techniques, since it provides three dimensional (3-D) real-space images with spatially localized measurements of structure and properties.

Depending on particular SPM, images can represent physical surface topography, electronic structure, or a number of other local properties. Under optimal conditions subatomic spatial resolution is achieved. When the sample is clean and flat, individual atoms can be imaged. SPM allows imaging at unprecedented levels of resolution without destroying samples. The first scanning probe microscope was the STM of Binnig and Rohrer [56]. STM is similar to a profilometer and image is obtained by scanning a tip over the surface of the sample and the motion control of the scanner is at the angstrom level. In STM, the tip does not make contact with the sample, while it is maintained at a height of 5 to 50 angstroms above the sample surface. Other SPM techniques are based

on the same scanner principles but use various detection schemes to access a wide range of properties, including atomic forces, electrostatic and magnetic forces, thermal gradients, and optical intensity. The development of the various scanning probe microscopy techniques has revolutionized the study of surface structure as atomic resolution images have been obtained not only on single crystal substrates in UHV, but also on samples at atmospheric pressure and even under solution.

SPM technologies share the concept of scanning an extremely sharp tip (3-50 nm tip radius) across the object surface. The tip is mounted on a flexible cantilever, allowing the tip to follow the surface profile. When the tip moves in proximity to the investigated object, forces of interaction between the tip and the surface influence the movement of the cantilever. These movements are detected by selective sensors. Various interactions can be studied depending on the mechanics of the probe. The most popular application of scanning probe microscopy is the study of molecules at the surfaces. The study of the surfaces depends not only on understanding the reactivity of the surface, but also on the underlying structure that determines reactivity.

### 2.1.1 Advantages of scanning probe microscopy

The resolution of SPM is not limited by diffraction, as in optical or electron microscopes but only by the size of the probe-sample interaction volume (i.e., point spread function), which can be as small as few picometers. The interaction can be used to modify the sample to create small structures (nanolithography).

### 2.1.2 Disadvantages of scanning probe microscopy

The scanning techniques are generally slower in acquiring images due to the mechanical scanning process. As a result, efforts are being made to greatly improve the imaging rate. The maximum image size is also generally smaller compared to other imaging techniques.

## 2.2 Types of scanning probe microscopy techniques

There are different SPM types, depending on the sensitivity and experimental conditions. Two most common scanning probe techniques are:

1. STM – Scanning tunneling microscopy
2. AFM – Atomic force microscopy

### 2.2.1 Scanning tunneling microscopy

The scanning tunneling microscope is widely used in both industry and academic research to obtain atomic-scale images of surfaces. It provides a three-dimensional profiles of the surface, which is very useful for characterizing roughness, observing surface defects, and determining the size and conformation of molecules and aggregates on the surface. Figure 2.1 shows the schematic view of an STM.

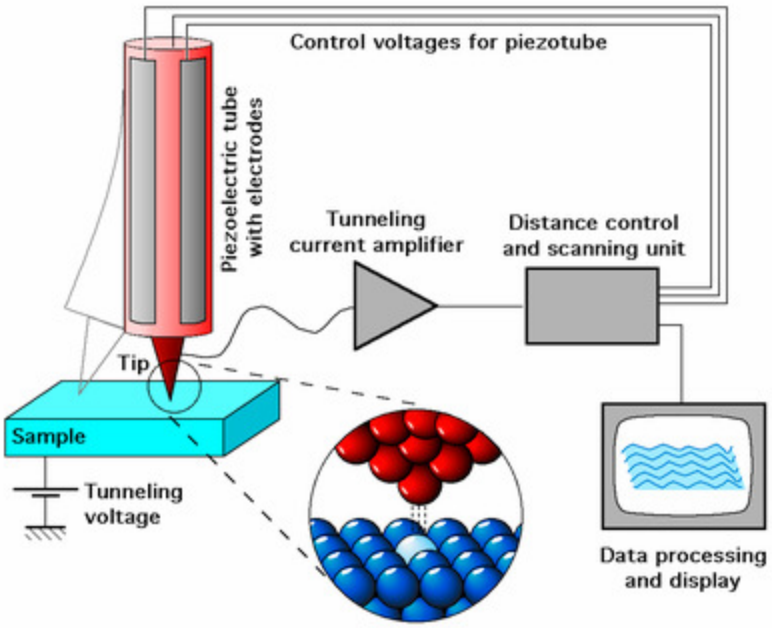


**Figure 2.1. Schematic view of an STM.**

The electron cloud associated with atoms at a surface extends a very small distance above the surface. When a very sharp tip is brought sufficiently close to such a surface, there is a strong interaction between the electron cloud on the surface and that of the tip, when an electric tunneling current flows between them due to a small applied voltage. At a separation of a few atomic diameters, the tunneling current rapidly increases as the distance between the tip and the surface decreases. This rapid change of tunneling current with distance results in atomic resolution if the tip is scanned over the surface to produce an image. If the tip is biased with respect to the surface by an application of a voltage between them, then electrons can tunnel between the two, provided the separation of the tip and surface is sufficiently small, which gives rise to the tunneling current. The name of this technique arises from the quantum mechanical tunneling-type mechanism by which the electrons can move between the tip and the substrate. Quantum mechanical tunneling permits particles to tunnel through a potential barrier which they could not

surmount according to the classical laws of physics. In this model, the probability of tunneling is exponentially dependent on the distance of separation between the tip and the surface. The tunneling current is therefore a very sensitive probe of this separation. To produce images, STM can be operated in two modes:

1. Constant height mode .

In this mode the tunneling current is monitored as the tip is scanned parallel to the surface. If the tip is scanned at a constant height above the surface, then there is a periodic variation in the separation distance between the tip and the surface atoms. At one point the tip will be directly above a surface atom and the tunneling current will be large whilst at other points the tip will be above hollow sites on the surface and the tunneling current will be much smaller. In this mode, constant height and constant bias are applied simultaneously as shown in Figure 2.2. A variation in the current results as the tip scans the sample surface because topographic structure changes the sample-tip separation. A plot of the tunneling current versus tip position therefore shows a periodic variation, which matches that of the surface structure, providing a direct image of the surface.

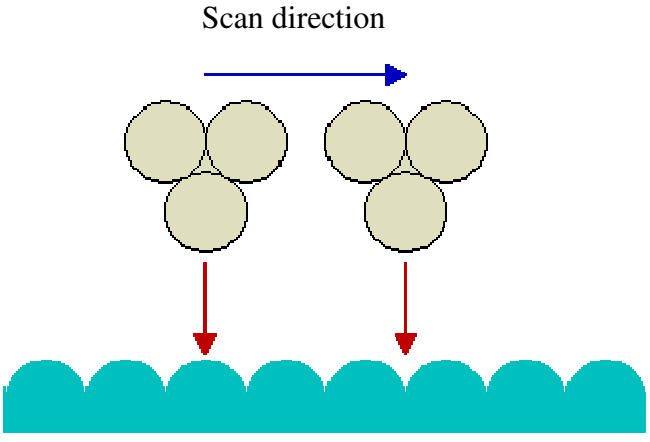


**Figure 2.2. Constant height imaging.**

2. Constant current mode.

In this imaging mode the surface tunneling current is maintained constant while the tip is scanned across the surface. This is achieved by adjusting the tip's height above the surface so that the tunneling current does not vary with the lateral tip position. In this mode the tip will move slightly upwards as it passes over a surface atom, and conversely, slightly in towards the surface as it passes over a hollow. The image is then formed by plotting the tip height (the voltage applied to the z-piezo) versus the lateral tip position. In constant current imaging, feedback mechanism is enabled to maintain a constant current while a constant bias is applied between the sample and the tip (Figure 2.3).

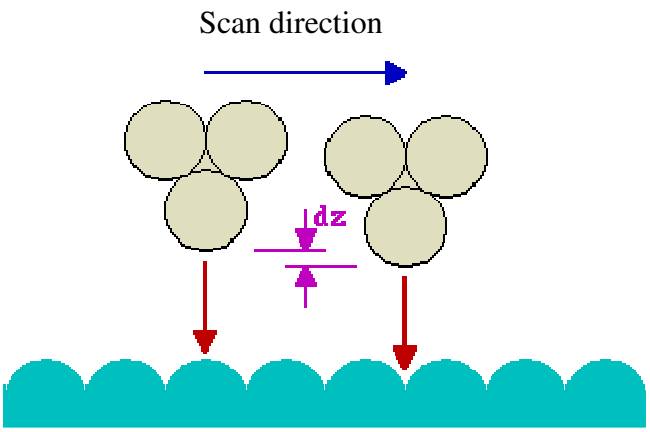


**Figure 2.3. Constant current imaging.**

### 2.2.2 Atomic force microscopy

The atomic force microscope (AFM) or scanning force microscope (SFM) was invented in 1986 by Binnig, Quate and Gerber [57]. Similar to other scanning probe microscopes, the AFM uses a sharp probe moving over the surface of a sample in a raster scan. In the case of the AFM, the probe is a tip at the end of a cantilever, which bends in response to the force between the tip and the sample. Because its operation does not require a current between the sample and the tip, AFM can be used to scan the non-conductive surfaces and can move into potential regions inaccessible to the scanning tunneling microscope, or image fragile samples which would be damaged by the STM tunneling current.

The basic objective of the AFM operation is to measure the forces at the atomic level between a sharp probing tip which is attached to a cantilever spring and a sample surface. Images are taken by scanning the sample relative to the probing tip and measuring the deflection of the cantilever as a function of lateral position. The AFM is being used to solve processing and materials problems in a wide range of technologies affecting the electronics, telecommunications, biological, chemical, automotive, aerospace and energy industries. The materials being investigating include thin and thick film coatings, ceramics, composites, glasses, synthetic and biological membranes, metals, polymers, and semiconductors which can be imaged in different environments such as liquids, vacuum and low temperatures. The AFM is being applied to studies of phenomenon such as abrasion, adhesion, cleaning, corrosion, etching, and friction. By using AFM one can not only image the surface at the atomic resolution but also measure the force at the pico-newton scale.

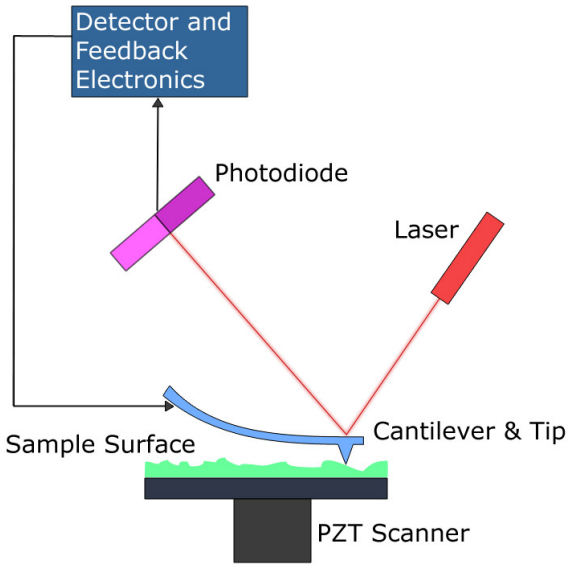


**Figure 2.4. Block diagram of an atomic force microscope.**

The above block diagram (Figure 2.4) explains the working principle of an AFM. AFM consists of a microscale cantilever with a sharp tip at its end that is used to scan the specimen surface. The cantilever is typically made of silicon or silicon nitride with a tip radius on the order of several nanometers. When the tip is brought into proximity to the sample surface, forces between the tip and the sample lead to a deflection of the cantilever according to the Hooke's law. Depending on the situation, forces that are measured in AFM include mechanical contact force, Van der Waals forces, capillary forces, chemical bonding, electrostatic forces, and magnetic forces. Typically, the deflection is measured using the position of a laser spot reflected from the top of the cantilever into an array of photodiodes. Other methods that are used include optical interferometry, capacitive sensing or piezoresistive AFM cantilevers. These cantilevers are fabricated with piezoresistive elements that act as a strain gage. Using a Wheatstone

bridge, strain in the AFM cantilever due to deflection can be measured, but this method is not as sensitive as laser deflection or interferometry. If the tip is scanned at a constant height, there is a risk that the tip would collide with the surface, causing damage. Hence, in most cases a feedback mechanism is employed to adjust the tip-to-sample distance to maintain a constant force between the tip and the sample. The sample is mounted on a piezoelectric tube that can move the sample in the $z$ direction for maintaining a constant force, and the $x$ and $y$ directions for scanning the sample. The AFM can be operated in three principal modes:

1. with feedback control
2. without feedback control
3. tapping mode

If the electronic feedback is switched on, then the positioning piezo which is moving the sample up and down can respond to any changes in force which are detected, and alter the tip-sample separation to restore the force to a pre-determined value. This mode of operation is known as constant force, and usually enables a fairly faithful topographical image to be obtained. If the feedback electronics are switched off, then the microscope is said to be operating in constant height or deflection mode. This mode is particularly useful for imaging very flat samples at high resolution. Often it is best to have a small amount of feedback-loop gain, to avoid problems with thermal drift or the possibility of a rough sample damaging the tip and/or cantilever. In tapping mode the cantilever is vibrated at a resonance frequency while being scanned above the sample

surface. This minimizes the shear force on the sample, thus allowing to image soft materials. Special compliant cantilevers are used for tapping mode operation.

## 2.3 Nanoindentation and in-situ imaging by Triboindenter

### 2.3.1 Nanoindentation

Nanoindentation techniques are widely used to determine the hardness and the elastic modulus of thin films for a variety of materials. In this method, load and indenter displacement are continuously recorded simultaneously during loading and unloading cycles [58]. The resultant load-displacement curve is then analyzed to determine hardness and elastic modulus. Conventional indentation hardness tests involve measuring of a residual plastic impression size on the sample surface as a function of indenter load, which provides contact area for a given indenter load. In nanoindentation tests, the size of the residual impression is very small and makes it difficult to measure directly using optical techniques.

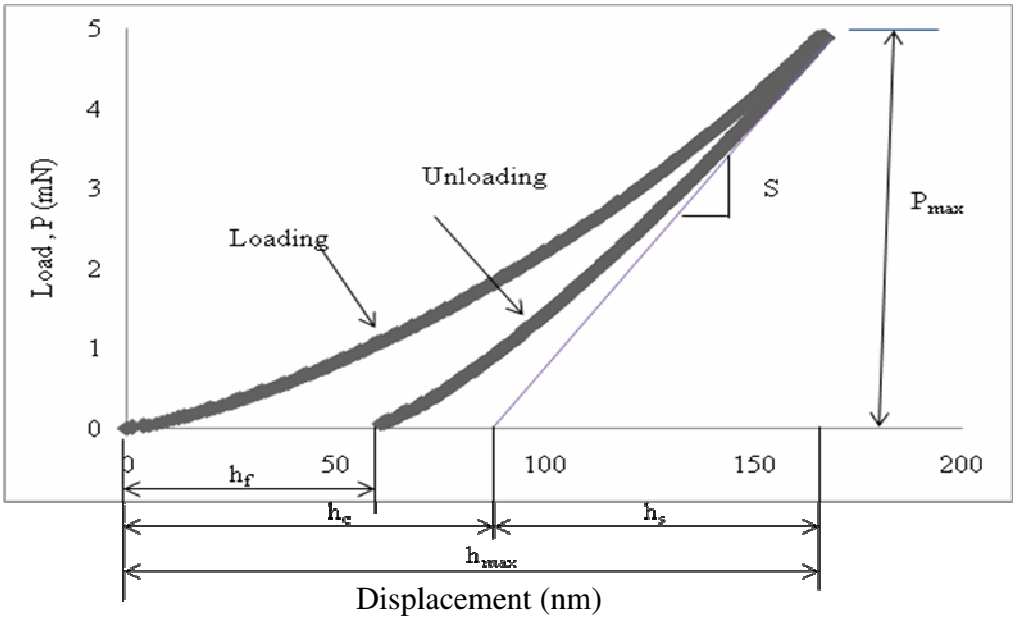


**Figure 2.5. Schematic representation of nanoindentation load-displacement curve.**

In nanoindentation testing, the depth of penetration is measured as the load is applied to the indenter. The known geometry of the indenter allows for the size of the contact area to be determined. Hardness of the material being tested is the ratio of the maximum indenter load to the contact area. This method also allows to measure elastic modulus by determining the sample stiffness. Stiffness is measured from the slope of the initial portion of the unloading curve. The widely used method to extract hardness and elastic modulus is established by Oliver and Pharr [59]. Figure 2.5 shows the schematic representation of nanoindentation load-displacement curve. The parameters in the diagram are used to analyze indentation data,

Where $S$ is the stiffness, i.e. slope of the unloading curve,

$P_{max}$ is the maximum load applied

$h_f$ is the final depth of penetration

Hardness (H) and elastic modulus (E) are measured from the following equations:

$$H = \frac{P_{\max}}{A} \tag{2.1},$$

where $A$ is the contact area at the maximum load, which is determined from the contact depth and geometry of the indenter tip.

$$E^* = \frac{\sqrt{\pi}}{2}\frac{S}{\sqrt{A_c}} \tag{2.2},$$

$$\frac{1}{E*} = \frac{1-\nu_S^2}{E_S} + \frac{1-\nu_{tip}^2}{E_{tip}} \tag{2.3},$$

where $E^*$ is the reduced modulus and in this method, elastic modulus of the sample depends on the deformation of the material and the testing device. $E_s$, $E_{tip}$, $\nu_s$, $\nu_{tip}$ are the elastic moduli and Poisson's ratios of the specimen, and indenter, respectively.

### 2.3.2 In-situ imaging using Triboindenter

In this work, Hysitron Triboindenter has been used to scan the calcite surface repeatedly. The Triboindenter is a versatile nanomechanical characterization tool designed to perform nanoindentation tests and in-situ imaging [60]. Piezo-scanner and three – plate capacitive transducer of this system enable it to perform surface scanning and nanoindentation tests. Figure 2.6 shows the Hysitron three plate capacitive transducer attached to the piezo scanner.

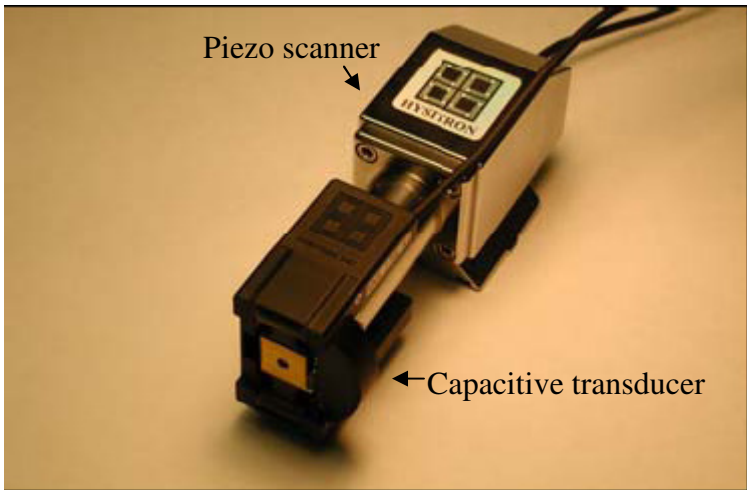


**Figure 2.6. Hysitron three plate capacitive transducer on the piezo scanner.**

The piezo scanner provides fine scale positioning of the indenter tip before and after indentations and is also used for surface imaging. When high voltage is applied to piezoelectric ceramics, its shape changes rapidly. To maintain constant volume, the dimensions will increase in one direction and decrease in other direction. Schematic of piezoelectric scanning tube is shown in Figure 2.7.

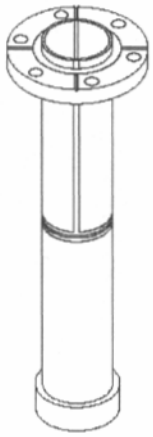

**Figure 2.7. Schematic of the piezo scanner ceramic tube.**

It is cylindrical in shape and has two halves. The top half of the tube consists of four separate quarters of the cylinder. Each quarter of the tube controls motion in +X, -X, +Y, and -Y directions. The bottom half of the scanner is made of a single piece of ceramic. When voltage is applied to the separate portion of the top half of the tube, it lengthens, causing bending, which translates into the lateral motion. When voltage is applied to lower half, it lengthens to provide motion along the Z-axis. By applying voltages to all five portions of the tube, 3D motion can be achieved. Three plate capacitive transducer is attached to the piezo tube in the Hysitron Triboindenter, and is used to apply load to the tip, while measuring the displacement of the tip during indentation.

### 2.3.3 Three plate capacitive transducer of the Triboindenter

The transducer of the nanoindenter pushes the tip into the sample and simultaneously monitors the indentation depth. The transducer consists of three plate capacitive force-displacement sensor. Schematic of the transducer is shown in Figure 2.8. Two pairs of capacitive plates, one for force actuation and the other for displacement detection, are combined and integrated into a three-plate transducer. The sensor consists

of two fixed outer electrodes i.e. drive plates, which are driven by AC signals, and a center plate. The electric field between the plates changes linearly as the two drive plates are parallel to each other and equally spaced from center plate. The potentials applied to the drive plates are always equal in magnitude but opposite in polarity at any instant. So the electric potential is maximized at the drive plates and is minimized at the center plate. The indenter tip is directly connected to the central plate and indentation depth can be obtained through measuring the displacement of the central plate relative to the two outer electrodes.

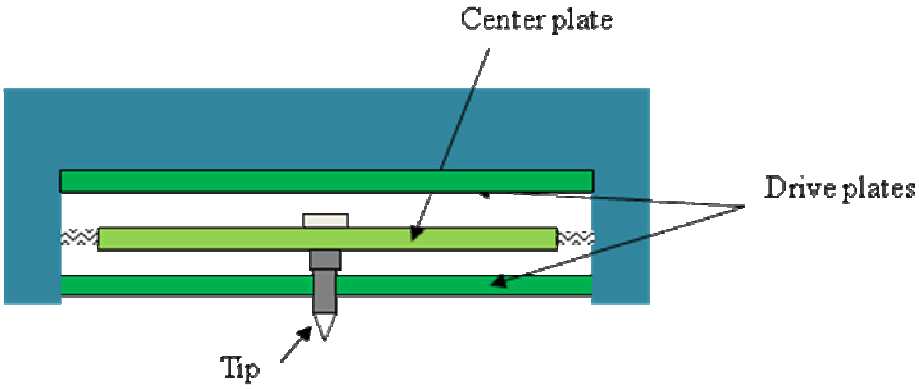


**Figure 2.8. Schematic of three plate capacitive transducer.**

The desired load is introduced by applying an appropriate voltage to the drive electrodes. To apply a load to the indenter, a large direct current bias is applied to the bottom plate and it will create an electrostatic attraction between the center plate and the bottom plate, which will pull the center plate down. The force can be calculated from the magnitude of the voltage applied to the drive plate. The central plate of the capacitive transducer is supported by several springs, whose spring constant is ≈150 μN/μm. Therefore an additional force will be introduced when the indenter tip is forced to move from its central position (e.g. 15 μN for 100 nm of displacement).

# Chapter 3

## Formation of Tip-induced Nanowear Ripples on Calcite Single Crystal

### 3.1 Tip-induced nanowear ripples

The repeated scanning of a material surface leads to the formation of the tip-induced wear patterns (nanoripples) consisting of ridges oriented perpendicular to the scanning direction. In general, wear is a rather complex process and efforts have been made to perform wear experiments under defined conditions. Particular way of simplifying wear experiments is performing them with a nanometer-sized tip sliding across the sample surface. AFM and a scanning Triboindenter are typical experimental tools to study nanowear.

The interaction between the tip of the scanning probe apparatus (AFM or the Triboindenter) and tested material surface is a complex process, which depends on material properties as well as on the scanning parameters. By changing the applied force and scanning speed, one can have different regimes of material wear caused by the tip. Wearless surface topography imaging is possible at low applied normal forces, while the tip damages the surface with increased load. The surface becomes rougher and bumps start to form. At even higher forces the tip removes part of the material. Repeated scanning over the same region magnifies this effect. When applying moderate forces in combination with repeated scanning over the same region, one could observe a periodic wavy pattern of ripples, which are oriented perpendicular to the direction of the tip

motion. Tip-induced wear patterns on single crystal calcite have been studied in this work using Hysitron Triboindenter.

### 3.2 Unit cell of calcite single crystal

Calcite has a chemical formula of $CaCO_3$, and is one of the most widely distributed minerals on the Earth. Figure 3.1 shows the rhombohedron crystal structure of the calcite.

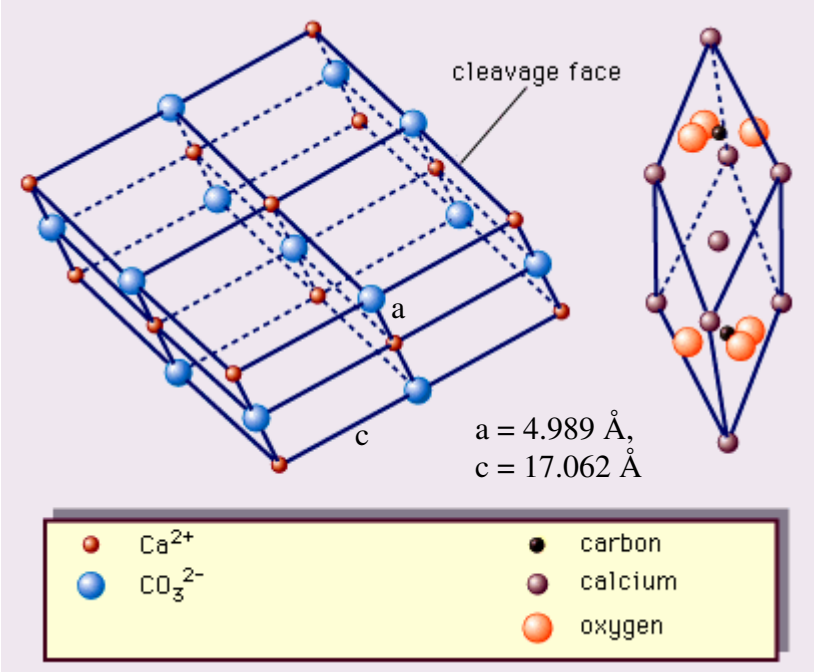


**Figure 3.1. The crystal structure of calcite.**

This schematic diagram shows both (left) the true unit cell (the acute rhombohedron, which contains 2[$CaCO_3$]) and (right) an alternative cell based on the cleavage rhombohedron. The carbonate groups break up the cubic symmetry in several ways. First, their three-fold symmetry axes line up with only one of the symmetry axes of

the cube. Second, they alternate in orientation. Most important, the wide spacing of the carbonate groups stretches the atomic planes and distorts the cube into a rhombohedron.

### 3.3 Experimental details

In this work, freshly cleaved natural calcite single crystal was scanned repeatedly in the ambient environment using Hysitron Triboindenter. This tool has the ability to scan the surfaces of the material continuously, while producing surface topography images. The piezo scanner of the Triboindenter provides the ability to scan 80 μm or less square area using rigidly fixed diamond tip. Density of scanning lines is always 256 lines per square area. Tip-induced wear patterns were observed as a function of scanning frequency (1 - 3 Hz) and normal load (2 – 8 μN) of the Berkovich diamond tip. Scanning speed of the tip depends on the frequency and the scan size. For 20 x 20 $\mu m^2$ scan size, velocity of the tip will be 120 μm/sec at 3 Hz. The Berkovich tip was used to scan the surfaces, which is a three-sided pyramid, having 143.5° included angle. Tip-induced wear was performed by repeated scanning of 20 x 20 $\mu m^2$ areas of the calcite surface at varying loads and frequencies. The tip moves along the horizontal axis forward and backward along the same line and then moves perpendicular to it and starts the next scan line. To study the tip-induced wear ripples, scan area was zoomed out to 40 x 40 $\mu m^2$ square to measure wear removal rate and ripple structure behavior after a few scans. At 3 Hz scanning frequency wear ripples started initiating at the first scan and propagated as the number of scans increased. Similar results were obtained on KBr and Al single crystals [61] in the ambient environment using the same system as well as using UHV-AFM on InSb [62] semiconductor. As the contact load increases beyond 6 μN, material started moving to the scan edges and ripple structure was never initiated. Similarly, at 1

Hz scanning frequency ripple structure was not initiated and wearing of the surface layer took place.

## 3.4 Results and discussion

As described in the previous section, the surface of the calcite layer was scanned repeatedly at 1 Hz and 3 Hz frequencies and at contact load of 2 - 8 µN with an increment of 2 µN in the ambient environment.

### 3.4.1 Tip-induced wear patterns at 3 Hz scanning frequency

#### 3.4.1.1 At a contact load of 2 µN

Initially surface of the calcite was scanned using the following parameters:

Scan Area = 20 x 20 µm square area

Frequency = 3 Hz (Velocity of the tip = 120 µm/sec)

Normal load on the tip = 2 µN

Figure 3.2, shows the topography image and the line profile of the calcite single crystal after the first scan. From the surface topography image, it is clear that the horizontal slope of the surface is ~200 nm over a 20 µm scan area. Ripples started initiating at the bottom of the surface slope during the first scan. As scanning continued, ripples propagated towards the other end of the scan edge, and the ripples orientation was perpendicular to the scan direction. One could see ripples on the whole surface with a periodicity of 2.3 µm after 10 scan cycles. Ripples started merging together from the $11^{th}$ scan and the rms roughness of the topography increased as the periodicity and height of the ripples increased.

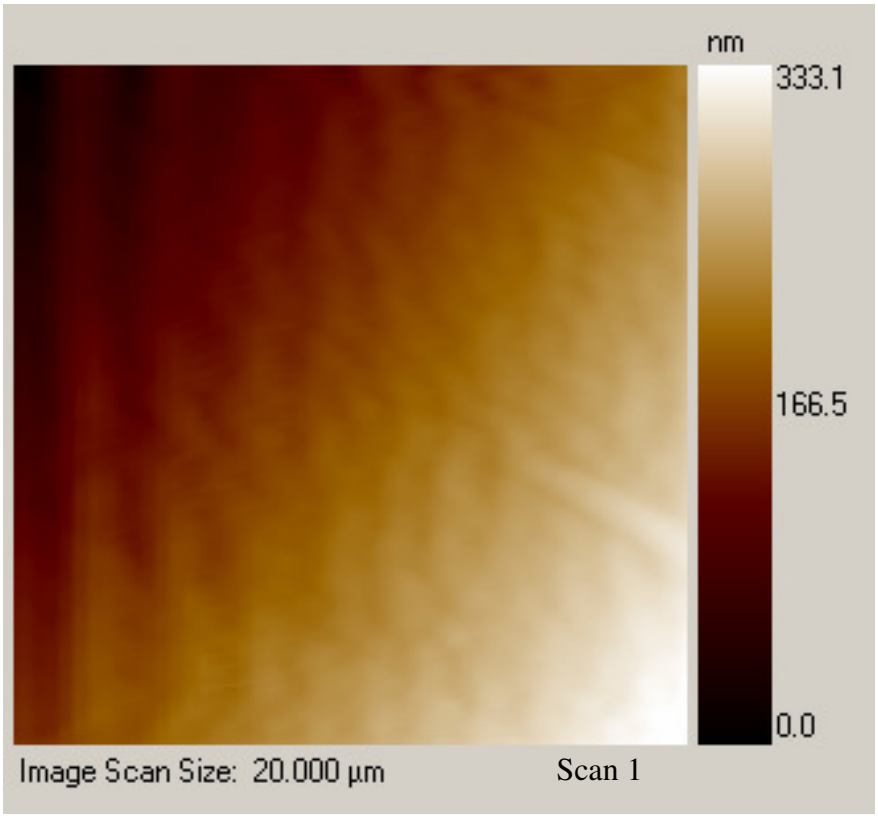


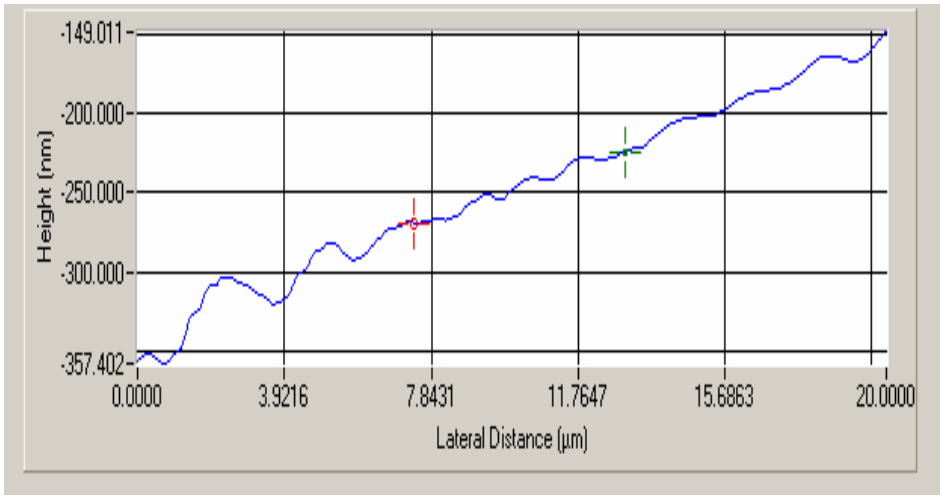


**Figure 3.2. Topography of the calcite surface at 3 Hz frequency and 2 µN normal load and its profile at the center after 1st scan, shows horizontal slope of the surface as ~200 nm over 20 µm.**

Figure 3.3 shows series of topography and gradient images of the calcite surface at the intermittent scans. As the number of scans increased, height of the ripples increased from 30 nm to 145 nm at the end of 130 cycles. Even after 130 scans, ripples with higher periodicity can be seen on the surface and top layer of the surface was not completely removed.

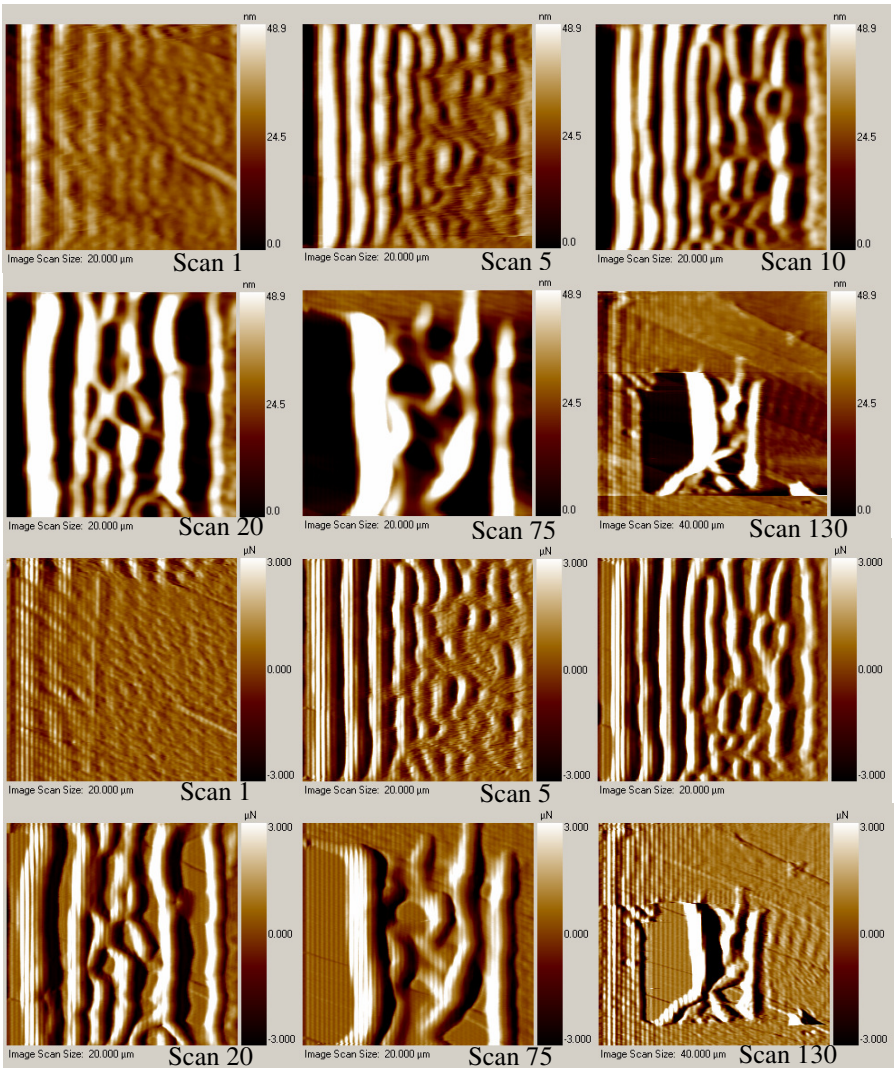


**Figure 3.3. Topography and gradient images of calcite after repeated scanning with the diamond tip, showing ripple initiation and propagation as scanning progressed at 3 Hz frequency and 2 µN normal load.**

### 3.4.1.2 At a contact load of 4 µN

In this case contact load of the tip is increased to 4 µN and the frequency is kept constant as 3 Hz. Figure 3.4 shows that the surface has the horizontal slope of 50 nm and ripples were not initiated during the first scan as in the previous case. As scanning continued, ripples started initiating at the bottom of the slope after 14 scans. These ripples were increasing in number and propagating towards the other scan edge as the number of scans increased.

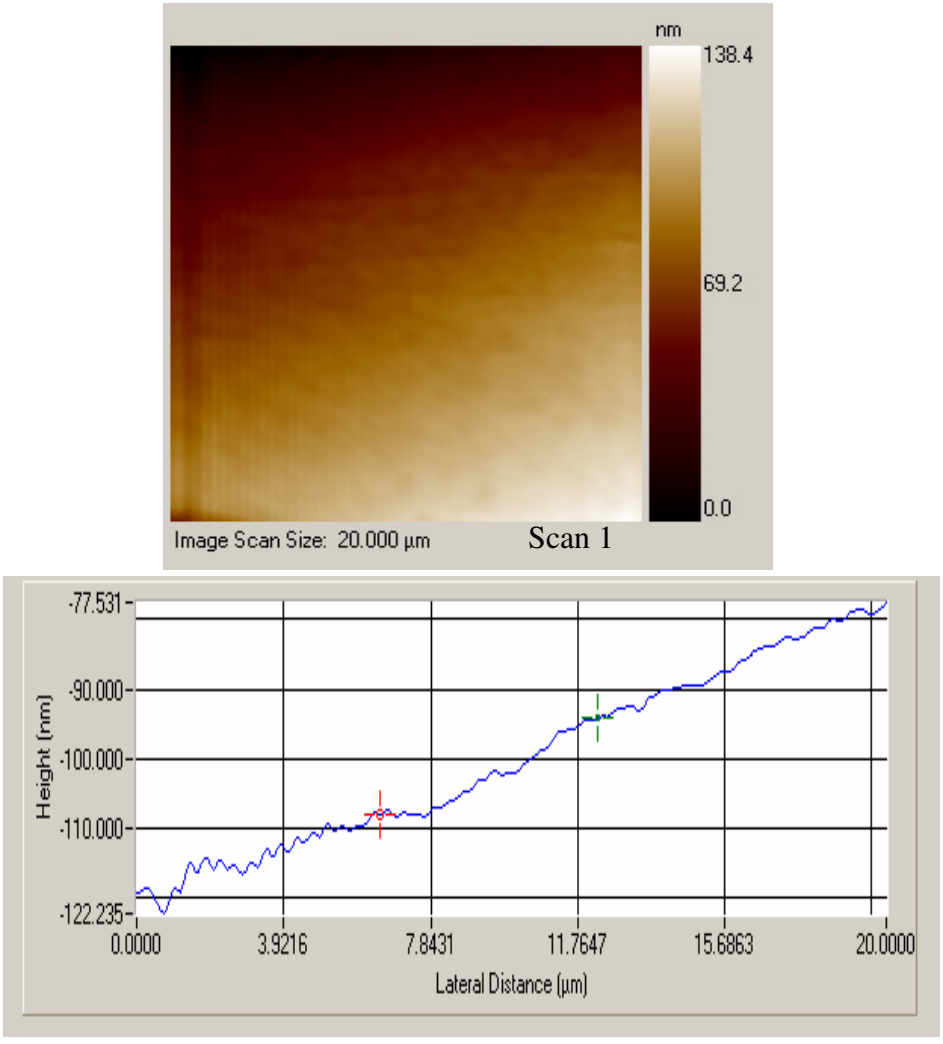


**Figure 3.4. Topography of the calcite surface at 3 Hz frequency and 4 µN normal load and its profile at the center after 1st scan, shows horizontal slope of the surface as ~50 nm over 20 µm.**

Periodicity of the ripples was 3.4 µm, and almost constant upto 100 scans. The height of the ripples increased from 59 nm to 72 nm at the end of 100 scan. Figure 3.5 shows series of topography and gradient images at intermittent scans of calcite single crystal. It was clear that ripples existed on the surface even after 100 scans at this load and frequency and new surface layer of the calcite did not appear.

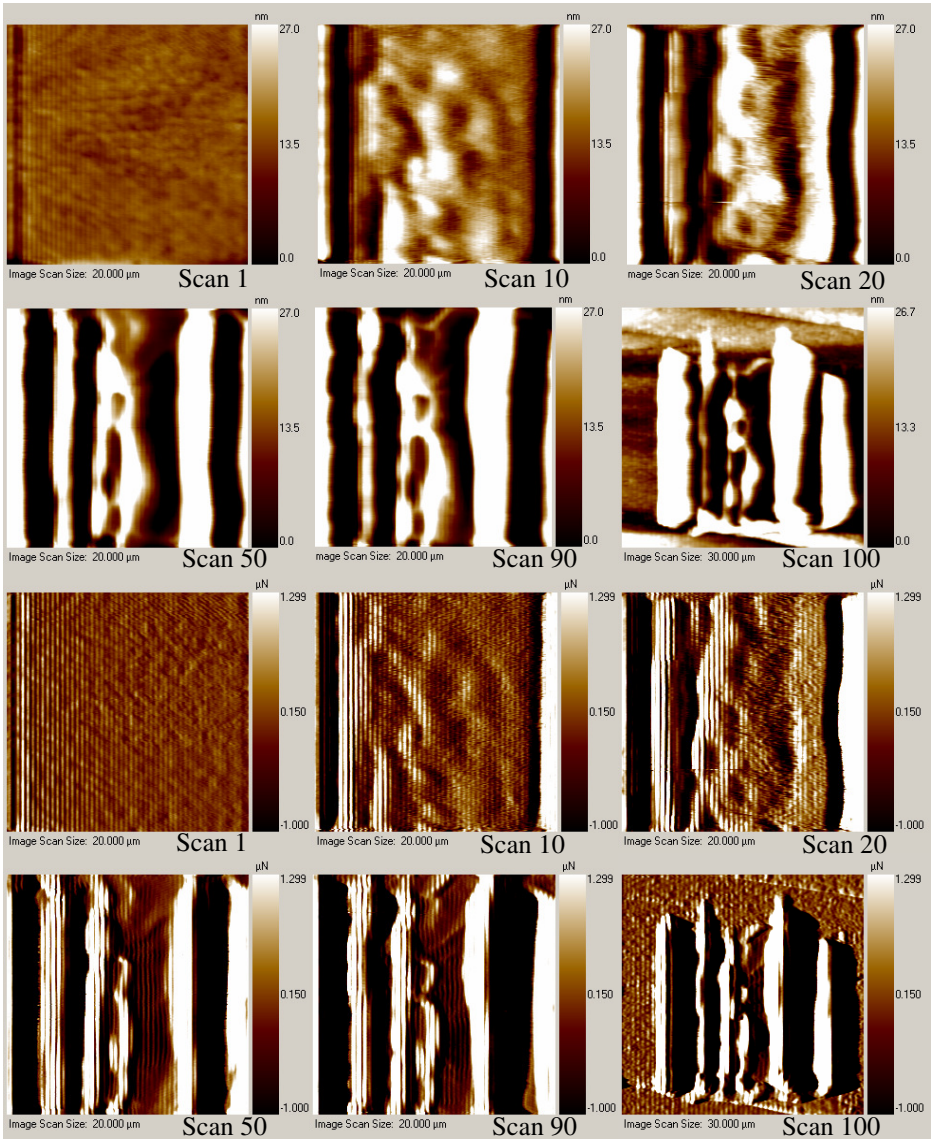


**Figure 3.5. Topography and gradient images of calcite after repeated scanning with the diamond tip, showing ripple initiation and propagation as scanning progressed at 3 Hz frequency and 4 µN normal load.**

### 3.4.1.3 At a contact load of 6 µN

Figure 3.6 shows the surface of calcite crystal with 86 nm horizontal slope over a 40 µm length and no ripples were initiated during the first scan. Ripples started initiating after five scans at the bottom of the horizontal slope of the surface and propagated towards the other scan edge as scanning continued. The initial ripple height was 55 nm and as scanning continued, ripples height decreased to 42 nm as wearing of the surface occurred.

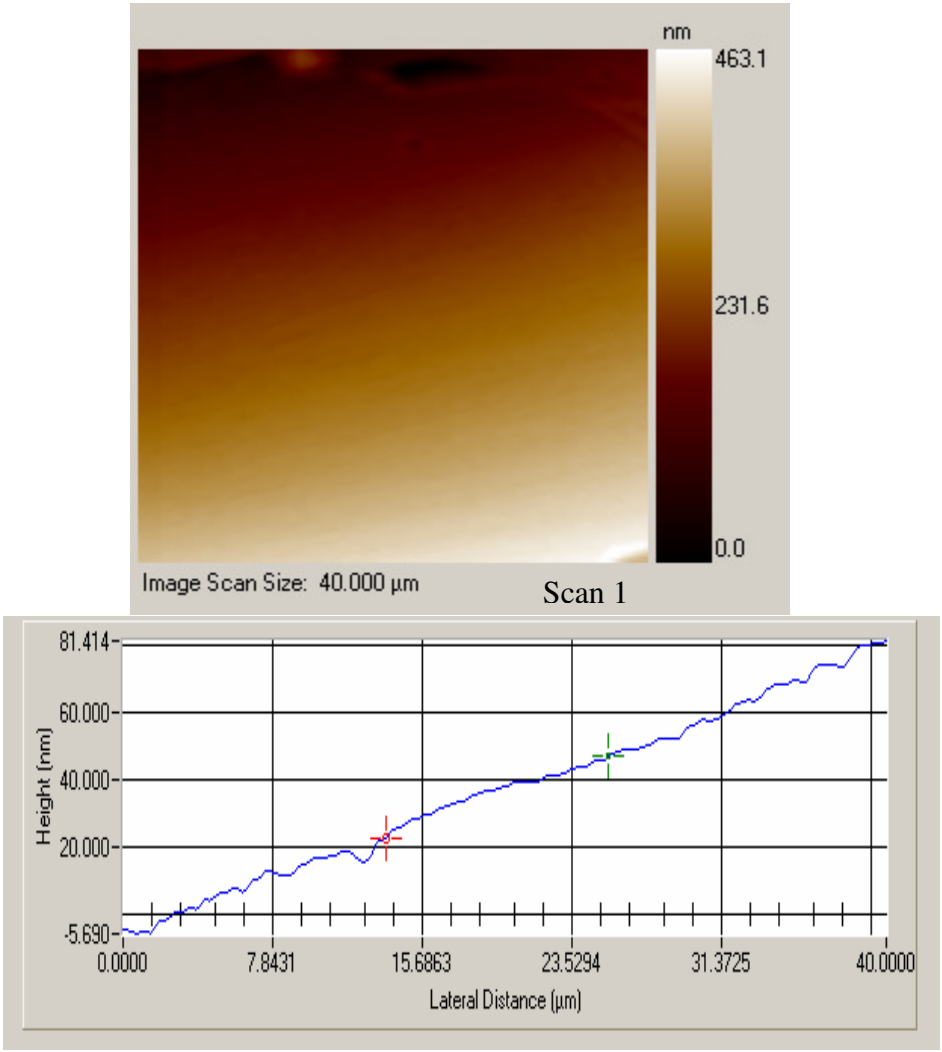


**Figure 3.6. Topography of the calcite surface at 3 Hz frequency and 6 µN normal load and its surface profile at the center after 1st scan which shows horizontal slope of the surface as ~86 nm over 40 µm.**

As the number of scans increased, the tip started removing the ripples while propagating ripples at the other end of the scan edge. One can clearly see material removal from the surface as the scanning progresses. Ripple periodicity decreased from 3.4 µm to 2.5 µm as scanning continued. After 28 scans, next surface layer of the calcite appeared and all the ripples were swiped away to the scan edges. Figure 3.7 shows series of topography and gradient images of the calcite crystal after intermittent scans.

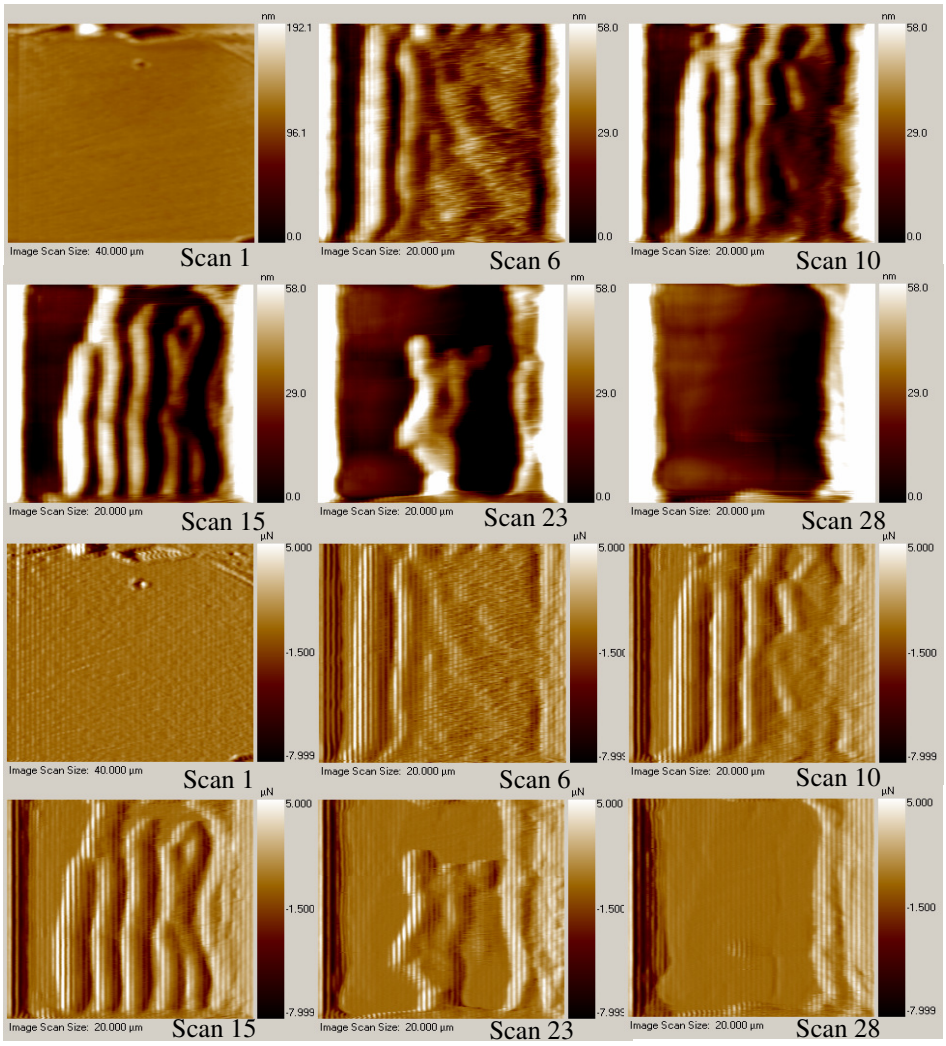


**Figure 3.7. Topography and gradient images of calcite after repeated scanning with the diamond tip, showing ripple initiation and propagation as scanning progressed at 3 Hz frequency and 6 µN normal load.**

### 3.4.1.4 At a contact load of 8 µN

As the load increased to 8 µN, tip-induced wear ripples were not initiated in the first scan. As the number of scans increased, tip started removing the surface layer of the calcite and moving it towards scan edges. No ripple structure appeared on the surface even after 25 cycles. After 30 scans, one can see a trench of 10 – 15 nm deep. Figure 3.8 shows the series of topography and gradient images of the calcite surface at this load.

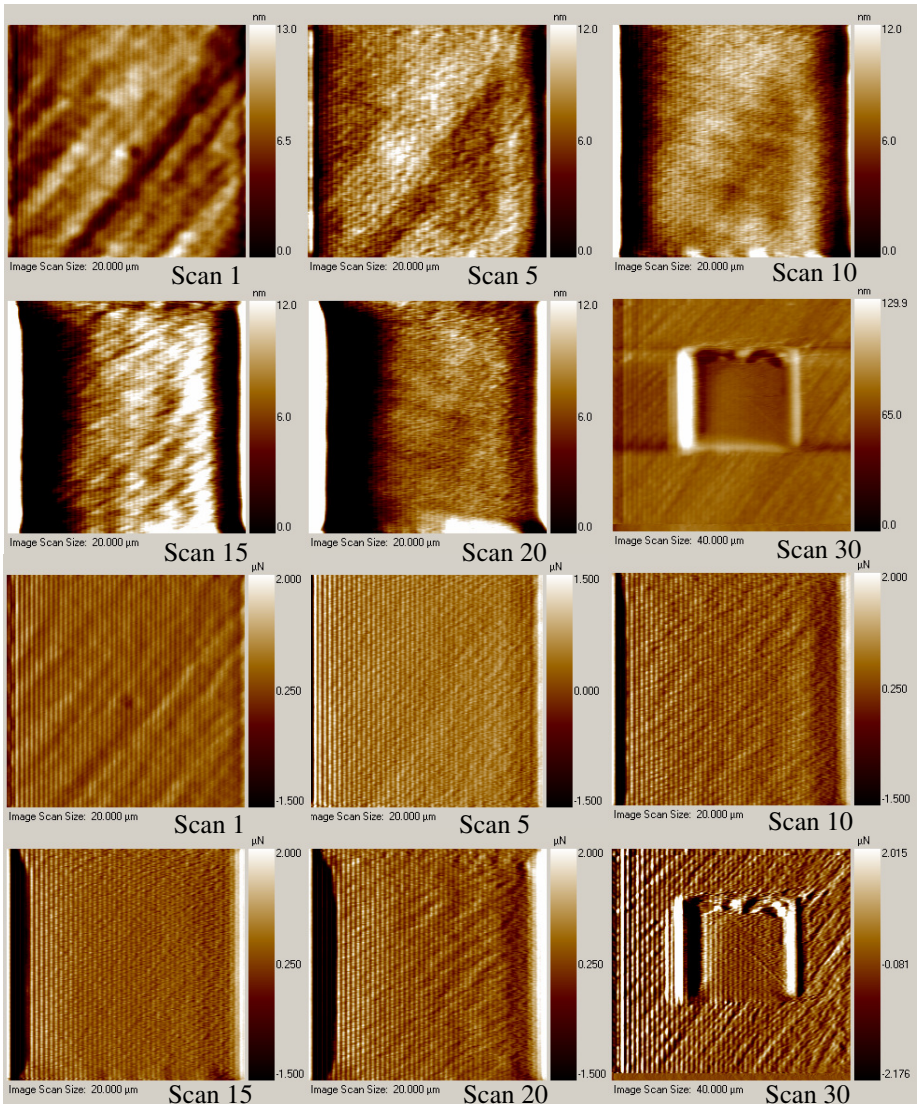


**Figure 3.8. Topography and gradient images of calcite after repeated scanning with the diamond tip at 3 Hz frequency and 8 µN normal load, showing a trench of 15 nm deep after 30 scans.**

### 3.4.2 Tip-induced wear patterns at 1 Hz scanning frequency

#### 3.4.2.1 At a contact load of 2 µN

Figure 3.9 shows the topography image of the calcite surface that has horizontal slope of 280 nm over 20 µm. As the scanning continued, the tip started removing the material from bottom of the slope instead of forming ripples on the surface.

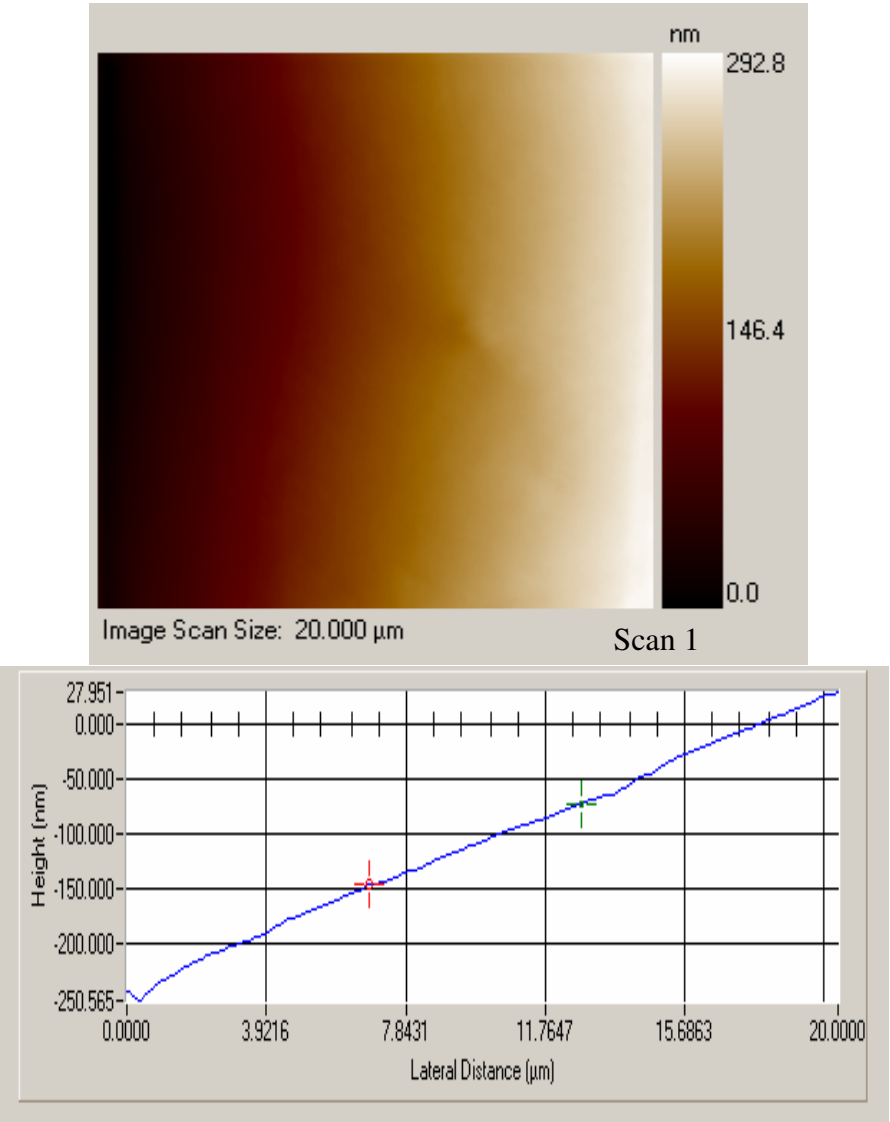


**Figure 3.9. Topography of the calcite surface at 1 Hz frequency and 2 µN normal load and its surface profile at the center after 1st scan which shows horizontal slope of the surface as ~280 nm over 20 µm.**

Top surface layer of the calcite was completely removed after 20 scans and no rippled structure could be seen on the surface. A trench, 15 nm deep can be seen after 20 scans at this frequency and load. Figure 3.10 shows the topography and gradient images of calcite surface as scanning progressed.

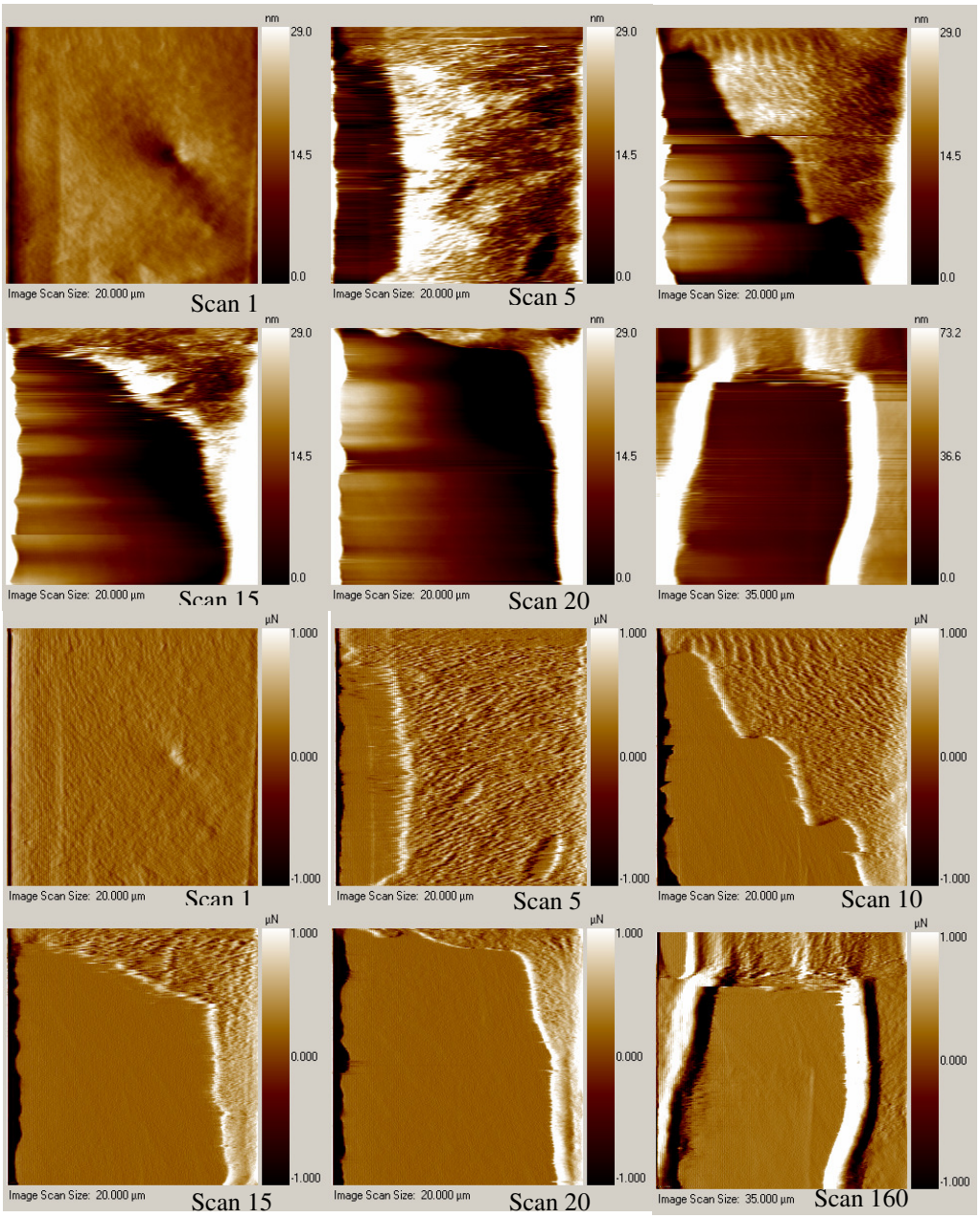


**Figure 3.10. Topography and gradient images of calcite after repeated scanning with the diamond tip at 1 Hz frequency and 2 µN normal load, showing a trench of 15 nm deep after 20 scans.**

### 3.4.2.2 At a contact load of 6 µN

As the load increased to 6 µN, the tip started removing the top layer of the calcite surface from the bottom of the slope and removed the layer completely within 10 scans. A new surface layer could be seen with less number of scans when compared to the previous case. Here, no ripple structures formed as the scanning continued. A trench of 15 nm deep can be seen after 10 scan cycles. Figure 3.11 shows series of topography and gradient images of calcite surface as scanning progressed.

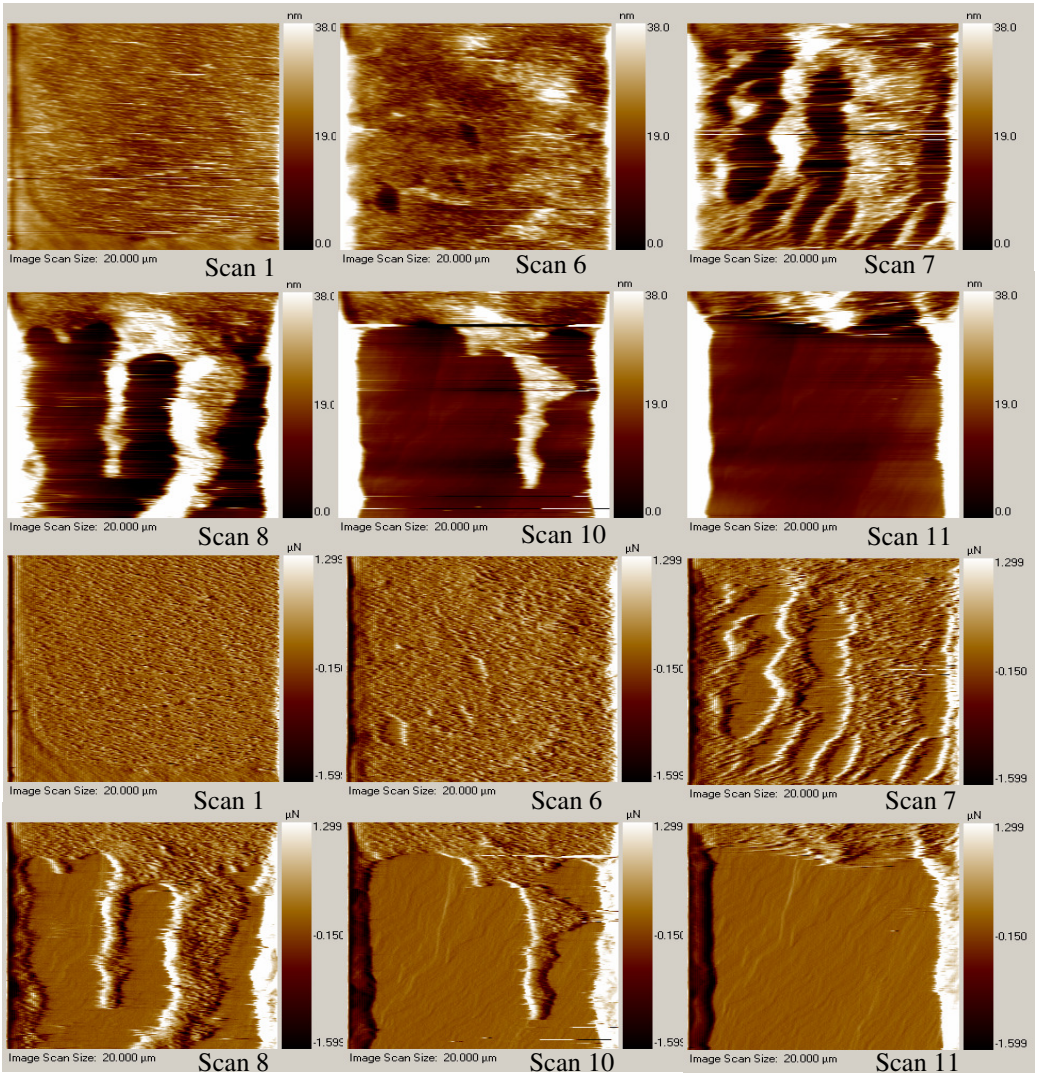


**Figure 3.11. Topography and gradient images of calcite after repeated scanning with the diamond tip at 1 Hz frequency and 6 µN normal load, showing a trench of 15 nm deep after 10 scans.**

### 3.4.3 Summary of wear tests

Tip-induced wear tests were performed on calcite single crystal by repeated scanning with the Berkovich diamond tip using Hysitron Triboindenter. Wear ripples were observed on the scanned surface at 3 Hz frequency over a 20 μm scan size with lower normal loads (≤ 6 μN), while material removal took place at 8 μN normal load. At 1 Hz frequency, the ripple structure did not initiate and tip removed the top layer of the surface after 20 scans at 2 μN normal load. Material removal rate increased as load increased to

6 μN, and 15 nm deep trench could be seen after 10 scan cycles.

### 3.4.4 Formation of tip-induced wear ripples and surface roughening

Formation of tip-induced wear ripples on single crystal calcite surface by Triboindenter was investigated by performing a series of experiments applying different contact loads and scanning speeds following the development of the structure with the number of scans. It was observed that ripple patterns formed on the calcite surface at contact loads of 2 μN, 4 μN, 6 μN at 3 Hz scanning frequency. When the surface of the calcite was scanned at the same 3 Hz frequency with 8 μN normal load, rippling structure was not developed and only wear of the surface took place. Even at the lower frequency of 1 Hz, rippling behavior was not observed and only removal of surface layer took place. Figures 3.3, 3.5 and 3.7 show the series of topography images with the number of scans at 3 Hz frequency and 2 μN, 4 μN, 6 μN contact loads, where the initial surface was relatively smooth and rms roughness was about 4.5 nm, 1.67 nm, and 5 nm respectively. As more scans were performed over the same region, the overall roughness increased and the surface morphology changed. When the same region is scanned over and over again

the height of the ripple patterns increased and started to merge to form periodic structures perpendicular to the scanning direction. The roughness of the ripple structures increased with the number of raster scans performed.

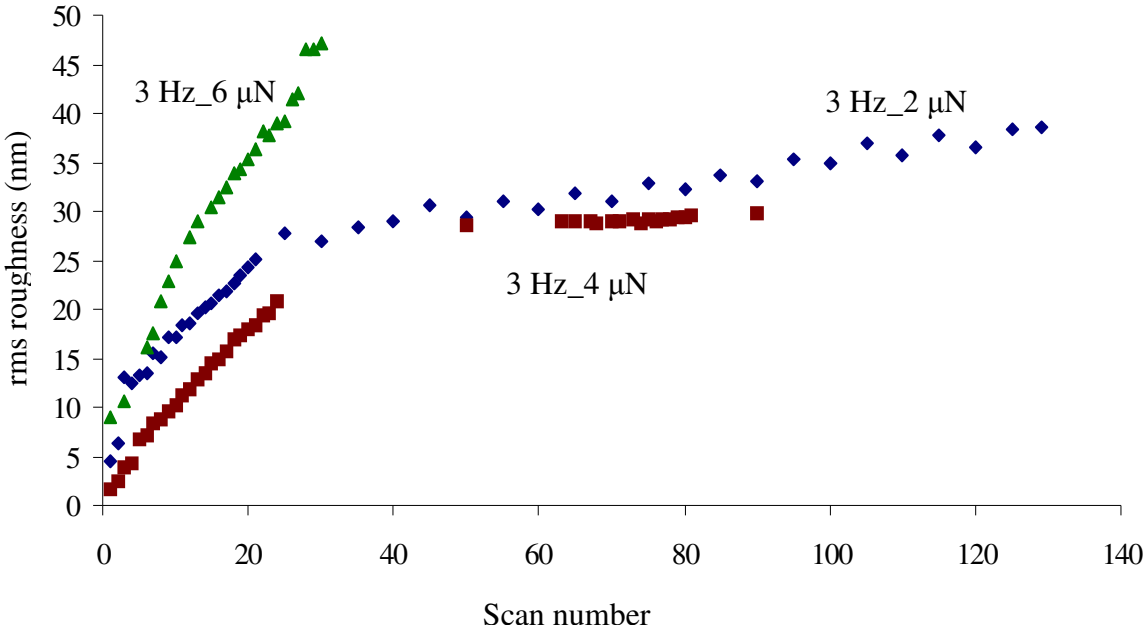


**Figure 3.12. RMS roughness of the surface topography of single crystal calcite with the number of scans at various contact loads at 3 Hz frequency.**

Figure 3.12 shows the rms roughness of the calcite surface topography with the number of scans. As the number of scans increased rms roughness increased and saturated after few cycles for the loads of 2 µN and 4 µN, which indicate that the ripple pattern initiated at the beginning and produced a fully developed structure as the number of scans increased. At these two loading conditions, wear of ripple structure was not seen as the number of scans increased. As the load increases to 6 µN, fewer scans are required to obtain a fully developed structure, and rms roughness did not get saturated. As the number of scans increased, the tip started breaking the ripple pattern and this stage

indicates the beginning of the transition between rippling and wear, which causes much faster increase of roughness. As the load increases further to 8 μN, rippling behavior did not initiate and only wear took place.

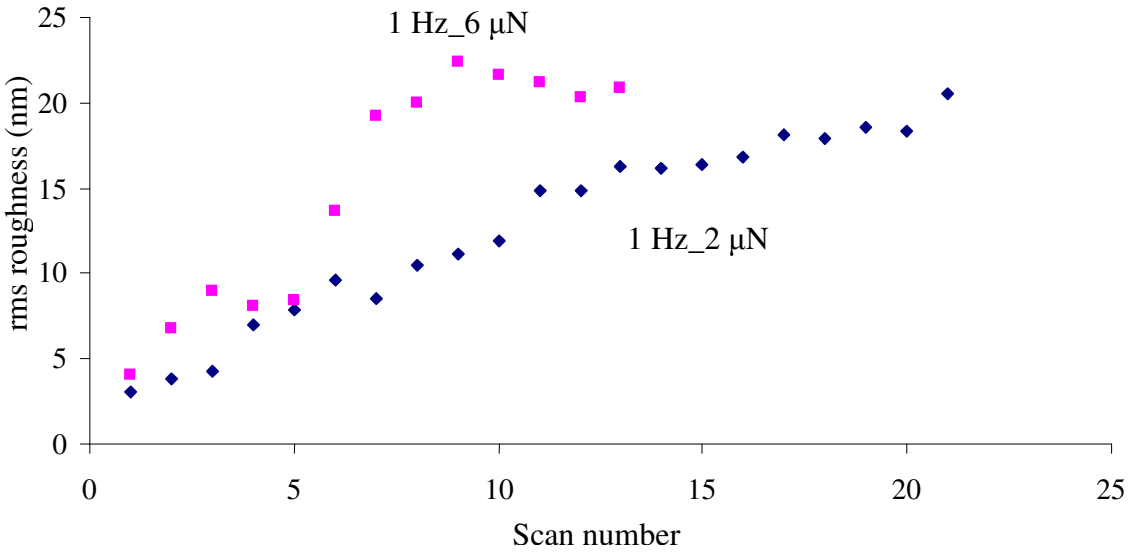


**Figure 3.13. RMS roughness of the surface topography of single crystal calcite with the number of scans at various contact loads at 1 Hz frequency.**

From Figure 3.13, rms roughness of the surface topography increased as the number of scans increased for both contact loads of 2 μN and 6 μN at 1 Hz. For 2 μN load, rms roughness was 20 nm after 21 scan cycles and for a load of 6 μN, surface roughness increased at a faster rate than in the earlier case within 10 scan cycles rms roughness was 22 nm and remained constant as the scans increases further.

### 3.4.5 Initiation and propagation of wear ripples

From the initial surface topography images, it is clear that the surfaces had horizontal slope in the range between 200 nm and 500 nm (Figure 3.2) for the 20 μm scan length. It was observed that in all cases ripples initiated and started propagating at the

bottom of the slope i.e. at the left side of the scan edge, which is attributed to the sample tilt (from Figure 3.2). Similar behavior was seen in KBr [21] in the ambient environment using Hysitron Triboindenter and on the InSb semiconductor surface in the UHV environment when scanned repeatedly with AFM [7]. The possible mechanism for the initiation of ripples is due to piezo hysteresis and surface slope. While the indenter is moving up along the surface slope, the piezo will work against gravity. Since the indenter scans the surface with constant velocity, the piezo takes little time to respond when indenter is in transition motion from forward to backward direction and vice-versa. This response time in the piezo could cause digging effect of the tip into the sample, which causes initiation of the ripple structure. As the ripple pattern behavior was observed at relatively high frequency of 3 Hz and removal of surface material occurred at lower frequency of 1 Hz, the self-excited vibration of the tip would have caused the ripples to propagate along the surface of the crystal. This phenomenon is equivalent to chatter observed at the macroscopic scale [61, 62].

### 3.4.6 Mechanical properties of single crystal calcite

Hardness and elastic modulus of the single crystal calcite were measured using the Hysitron Triboindenter with the diamond tip. In this measurement, partial loading and unloading cycle was used to measure these properties at different depths. Figure 3.14 shows the partial loading and unloading cycle for nanoindentation. Figures 3.15 and 3.16 show hardness and elastic modulus as a function of indentation depth. At lower depths (<100nm), hardness decreased from 3.1 GPa to 2.6 GPa and became constant as the penetration depth increased. Elastic modulus of the calcite increased from 62 GPa to 73 GPa upto 50 nm depths and remained constant as the penetration depth increased.

Hysteresis in the load-displacement curves is attributed to the possible energy dissipation due to plastic deformation.

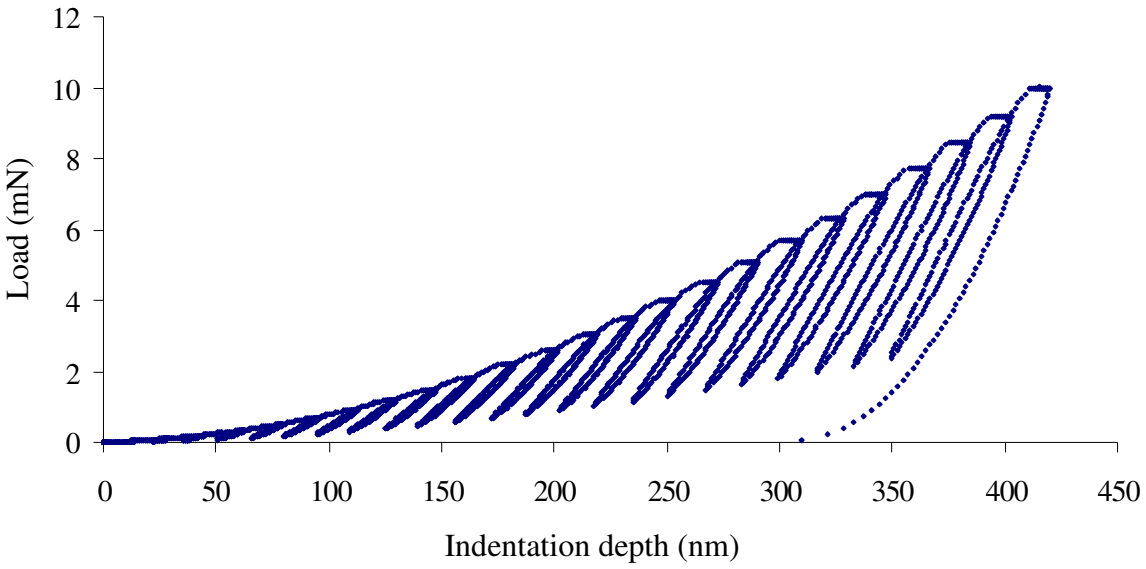


**Figure 3.14. Load–displacement behavior of single crystal calcite when loading and unloading is partial during the nanoindentation.**

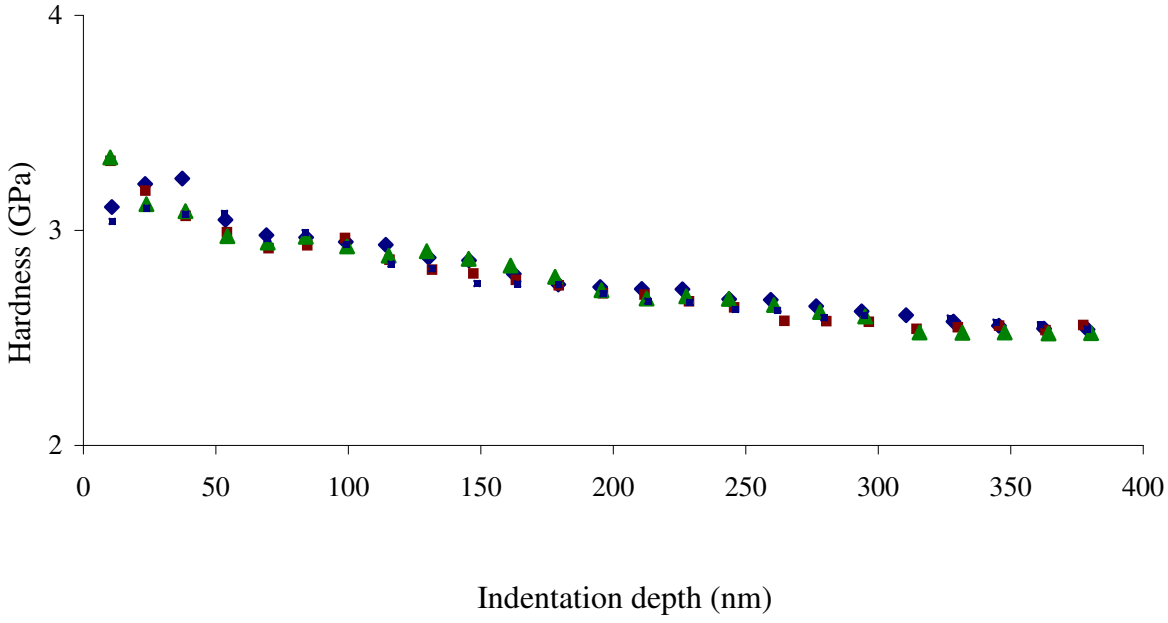


**Figure 3.15. Hardness of the calcite single crystal with depth of penetration.**

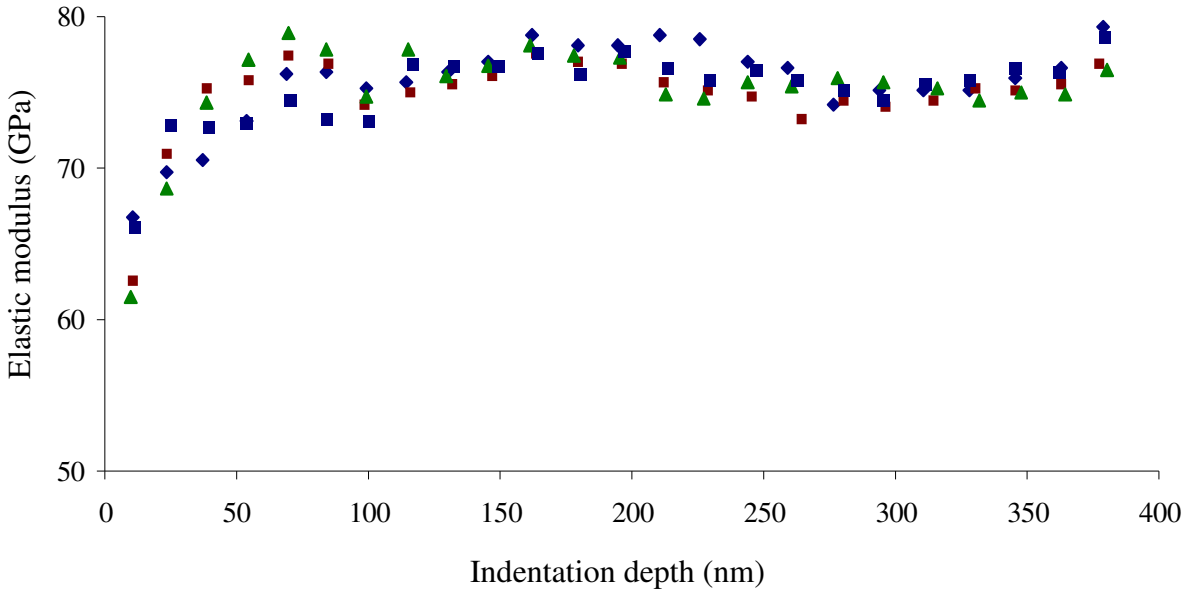


**Figure 3.16. Elastic modulus of the calcite single crystal with depth of penetration.**

In this chapter, formation of nanoripples was studied by scanning the surface of the calcite repeatedly with the diamond tip using Hysitron Triboindenter in the ambient environment. Tip-induced wear behavior was studied with the function of normal load and scanning frequency. The following chapter discusses, $Ar^+$ ion-induced nanostructures or nanoripples on InP (100) single crystal in the UHV environment. Scanning tunneling microscope (STM) was used to evaluate the surface morphologies after $Ar^+$ ion bombardment.

# Chapter 4

## Nanostructuring of InP (100) Single Crystal by $Ar^+$ Ion Bombardment

### 4.1 Ion-beam induced nanopatterning of InP

The formation of nanostructures on semiconductor surfaces has attracted much interest due to their potential applications in optoelectronic devices and as templates for growing nanostructures. Self-organization of nanostructures by ion bombardment offers an attractive solution because of its compatibility and reproducibility with easily controllable fabrication conditions. Nanopatterning by conventional lithography can create uniform nanostructures but it is costly and production rate is lower for large-scale fabrication. Although various methods are available to form complex topographic structures at the sub-micron to nanometer levels, ion bombardment is still a powerful, realistic and fast method to create nanostructures.

Among the III-V compound semiconductors, Indium Phosphide (InP) is known for its extraordinary roughness development during ion bombardment and is a very important component in wireless communications and optoelectronics industries. Due to its outstanding electrical properties such as high electron mobility and high breakdown voltage, InP is widely used as a substrate material in optical fiber communication systems, and in high frequency and high power device systems. By varying different irradiation parameters i.e. ion flux, incident ion energy, ion fluence, angle of incidence and substrate temperature, different structures can be formed, including nanodots, nanowires, nanospikes and nanoripples, etc.

## 4.2 Experimental procedure

The commercially polished InP (100) from Kelpin Crystals (Neuhausen, Germany), 5 x 5 mm in size was tightly clamped on a molybdenum plate. The molybdenum plate was connected to the copper block, which can be heated upto 1000 K by a resistive heater fixed inside the copper holder. The sample temperature is measured on the copper block by a chromel-alumel thermocouple. The experimental system consists of three interconnected UHV chambers, which include sample preparation chamber, transfer chamber, and surface analysis and imaging chamber. The base pressure in this system is 5 x $10^{-11}$ Torr. The sample preparation chamber is used to clean the copper sample holder and samples, and for ion irradiation. After samples irradiation of substrates in the preparation chamber, they are transferred to the surface analysis chamber through a transfer chamber, where analysis of the surface topography takes place using scanning probe microscopy.

Copper block sample holder was heated at $500^{o}$ C for 1 hour, before loading the InP substrate, in order to remove the moisture and contaminating oxides present on the copper block. Initially, the substrate surface was cleaned with a raster 0.5 KeV $Ar^{+}$ ion beam, bombarding surfaces at alternating incidence angles ($-60^{0}$ and $+ 60^{0}$ off the normal) for approximately 2 hours. The substrate is kept at a temperature of 650 K during ion beam bombardment. The substrate was annealed at 750 K for two hours following the ion sputtering. The above procedure was conducted several times to ensure that clean and flat surface was achieved before performing ion sputtering for surface modification studies. Various parameters in the ion sputtering are ion energy ($E$), incidence angle ($\Phi$), ion fluence ($\varphi$), ion flux (average current density, $J$) and temperature ($T$) of the substrate.

In this work, we have studied the effect of ion fluence on the nanostructures formation on the InP (100) single crystal surface by $Ar^+$ ion bombardment by keeping the ion flux and the incident energy constant. Ion-induced surface modifications were performed in subsequent cycles with 3 KeV $Ar^+$ focused ion beam, having average current density, i.e. ion flux in the spot of 4.25 x $10^{12}$ ions/cm$^2$/sec. The ion flux, was measured as a ratio of the total ion beam current to the area of the beam spot determined from the beam profile. The beam spot area was changed in the range of 0.3 – 0.9 cm$^2$. The ion beam incidence angle was 75$^o$ with reference to the surface normal. Ion fluence in the range between 7.7 x $10^{13}$ and 4.56 x $10^{17}$ ions/cm$^2$ was applied. The InP substrate was kept at room temperature during the ion beam sputtering. The sputtering was done in the raster mode to avoid crater edge effects [68]. The pressure before starting ion bombardment was about 2 x $10^{-9}$ Torr and was kept at $10^{-8}$ Torr during the sputtering by letting a turbo pump run throughout the experiment.

The modified surfaces of InP substrates were studied using STM under UHV conditions at room temperature. The pressure during the surface evaluation was maintained at 5 x $10^{-12}$ Torr. It is known that surface roughness depends on the scale [63] and fixed scan sizes of 1x1 μm was used for all measurements. The resolution, i.e. number of pixels for each image was always 500 x 500. We described the fluence dependence of topography in terms of surface root mean square roughness (RMS) and the average wavelengths of the surface nanostructures. The nanostructures wavelength was measured from the self-correlation functions of the images.

## 4.3 Results and discussion

In Figure 4.1, the STM image of the InP surface topography and its surface profile are shown after surface cleaning by $Ar^+$ ion sputtering for 2 hours at ion energy of 0.5 KeV and at $60^o$ angle to the surface normal, followed by annealing at 750 K for 2 hours. This surface had received ion bombardment with various ion fluences. Image topography shows that surface is uniform, clean and smooth, having RMS roughness of 0.28 nm. Since the surface was bombarded with $Ar^+$ ions, it started creating nanostructures in the form of nanodots and elongated surface protrusions, which are parallel to the ion beam.

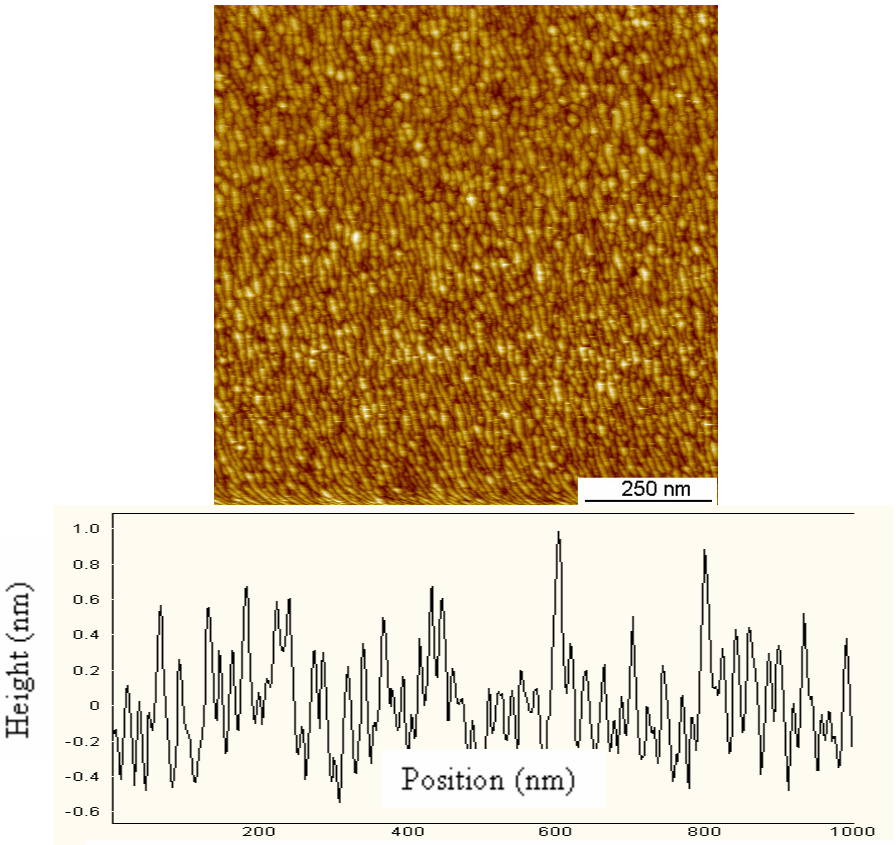


**Figure 4.1. STM image of 1 x 1 μm surface topography of InP (100) after surface cleaning by $Ar^+$ ion sputtering, followed by annealing for 2 hrs and its average surface profile of the image showing RMS roughness of 0.28 nm.**

Figure 4.2 shows auto-correlated surface topography image after ion sputtered cleaning followed by annealing, along with its profile, indicating that the wavelength of nanostructures is about 12 nm. Autocorrelation is a mathematical tool and is useful for finding repeating patterns in the topography image and determines the presence of any periodic patterns which have been buried under noise.

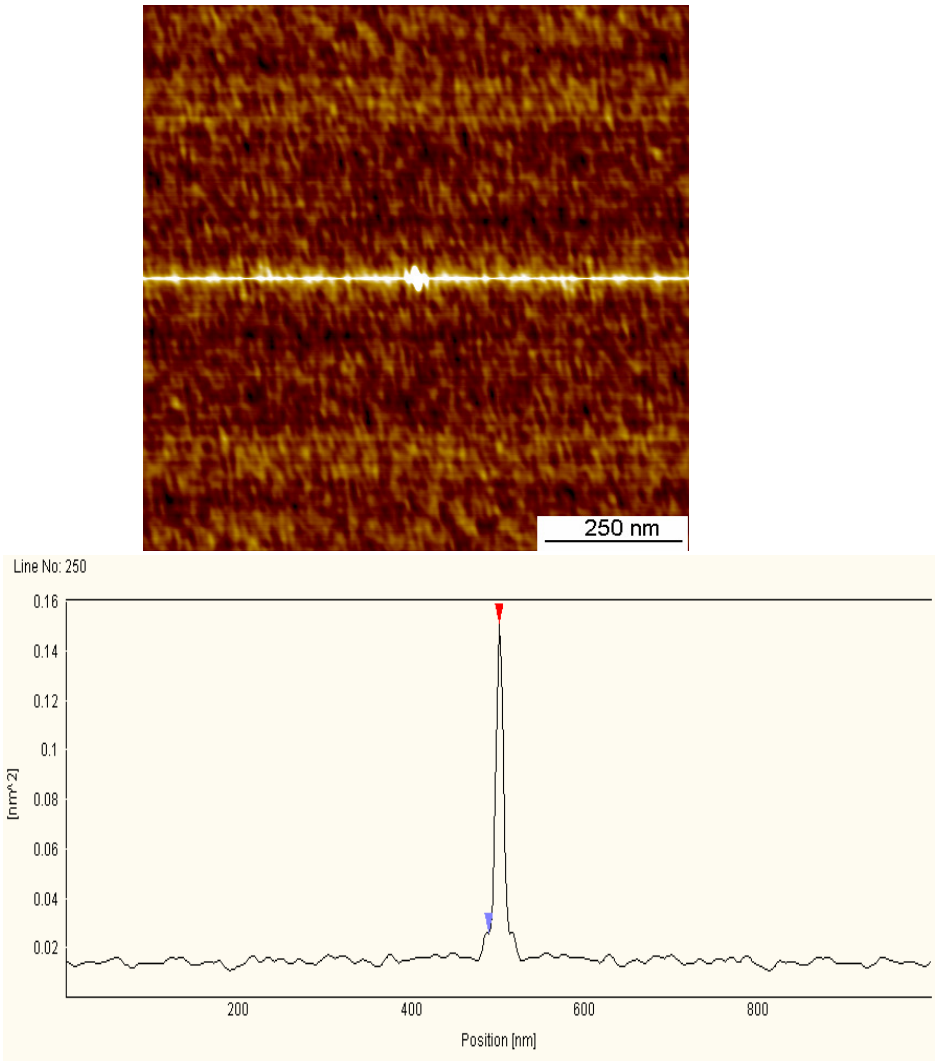


**Figure 4.2. Auto correlated image of InP (100) after surface cleaning by $Ar^+$ ion sputtering followed by annealing for 2 hrs and its profile at the center of the image, showing wavelength of 12 nm.**

Figure 4.3 shows STM surface topography image and its profile after bombarding at ion fluence of 7.7 x $10^{13}$ ions/cm$^2$ with an incident ion energy of 3 KeV at 75$^o$ to the surface normal. In this case, small nanodots disappeared and combined together to form elongated structure resembling small sized nanoripples. Average surface profile of the image shows that RMS roughness increased to 0.35 nm and wavelength of these structures also increased to 14 nm.

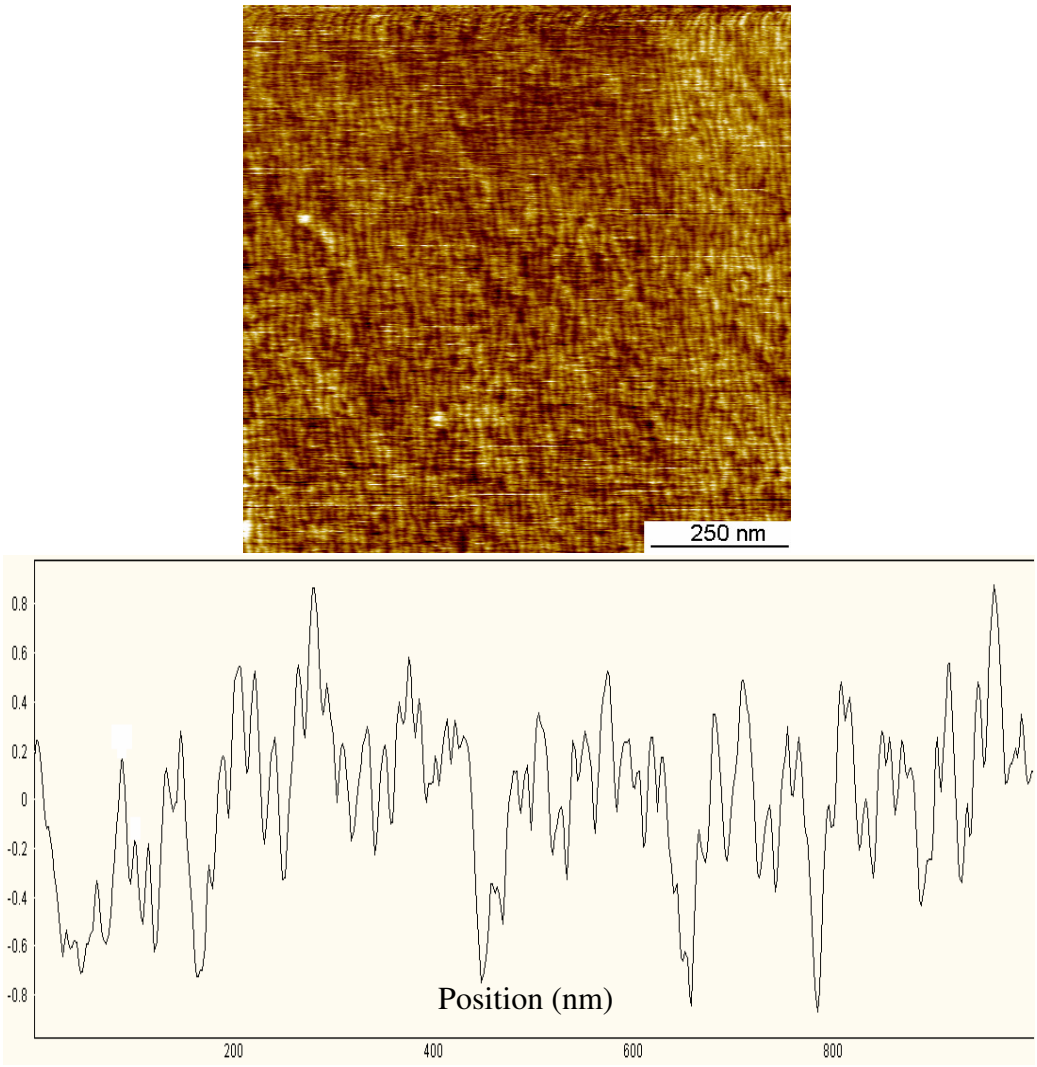


**Figure 4.3. STM image of 1 x 1 µm surface topography of InP (100) after $Ar^+$ ion bombardment at ion fluence of 7.7 x $10^{13}$ ions/cm$^2$ and its average surface profile of the image showing rms roughness of 0.35 nm.**

From the STM image and its average surface profile in Figure 4.4, it is evident that nanoripples are propagated uniformly throughout the image and are parallel to the direction of the incident ion beam. In this case RMS roughness is increased to 0.434 nm. Wavelength of these nanoripples can be found from the autocorrelation image and is increased to 24 nm, which is approximately doubled from the previous case.

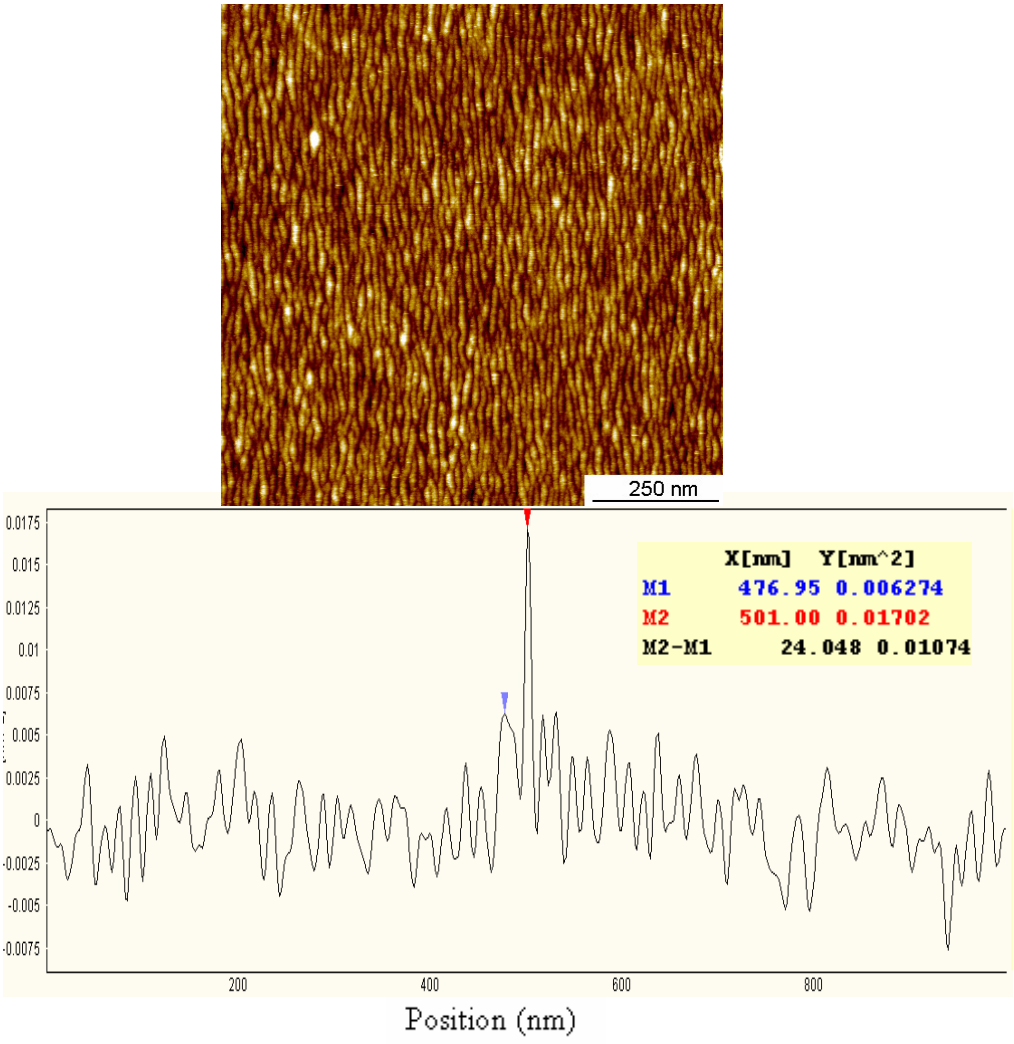


**Figure 4.4. STM image of 1 x 1 μm surface topography of InP (100) after $Ar^+$ ion bombardment at ion fluence of 4.6 x $10^{14}$ ions/$cm^2$ and its profile at the center of the self-correlated image, showing wavelength of 24 nm.**

As irradiation continued, at ion fluence of 1.05 x $10^{16}$ ions/cm$^2$, surface topography of InP (100) changed drastically and the ripple size increased. In this case, surface morphology is converted to a series of nanodots from regularly arranged nanoripples pattern. From Figure 4.5, it is clear that nanodots (50 – 80 nm in diameter) were merged together in a series along the incident ion beam direction to form nanoripples, which are prominent and larger in size. The RMS roughness of 7.89 nm was measured from the average surface profile. The wavelength of these nanoripples is 124.25 nm measured from the auto-correlated image.

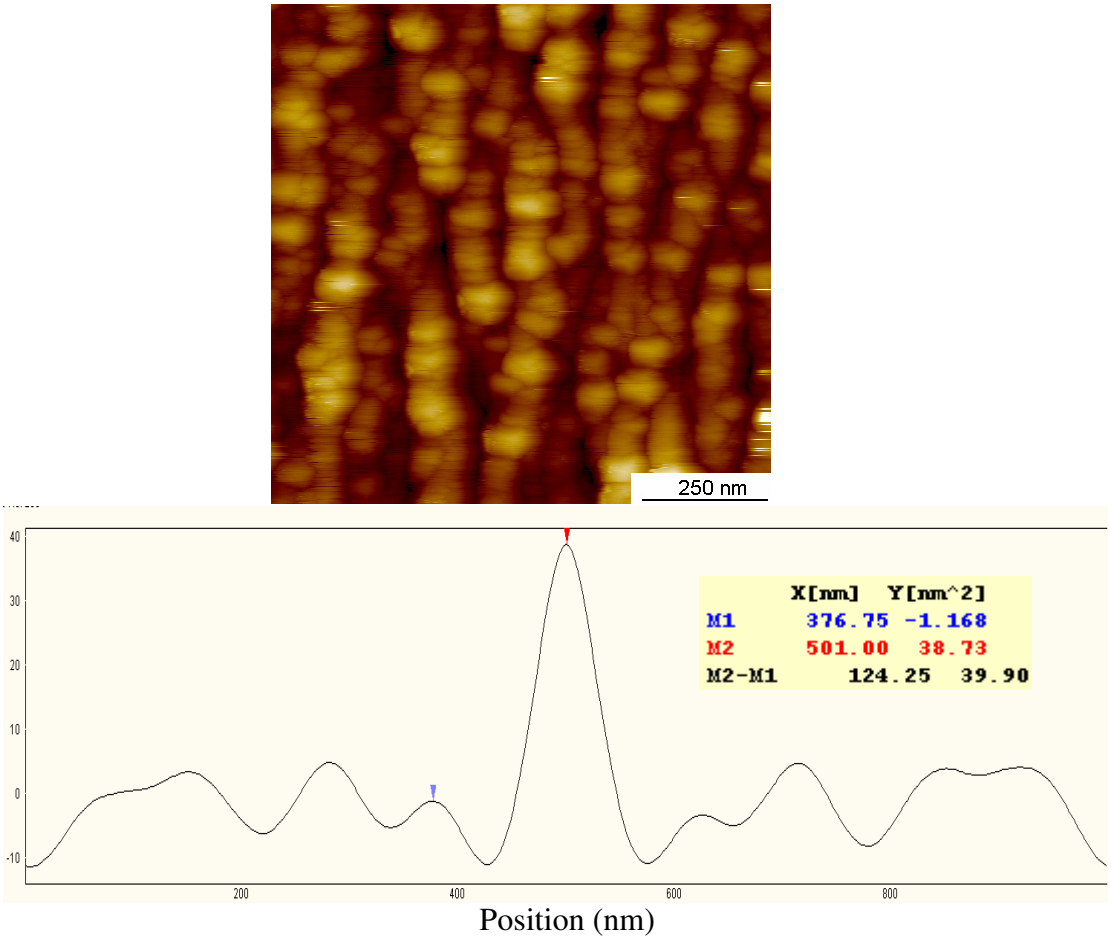


**Figure 4.5. STM image of 1 x 1 µm surface topography of InP (100) after $Ar^+$ ion bombardment at ion fluence of 1.05 x $10^{16}$ ions/cm$^2$ and its profile at the center of the self-correlated image, showing wavelength of 124 nm.**

As irradiation progressed by increasing the ion fluence to five times than in the previous case ($\varphi$ = 5 x $10^{16}$ ions/cm$^2$), size of the nanodots (75 – 125 nm) increased further (Figure 4.6) and merged together along the direction of the incident ion beam to form the nanoripples pattern. At this fluence RMS roughness of the surface increased to 10.6 nm and the nanoripples wavelength increased to 316.63 nm.

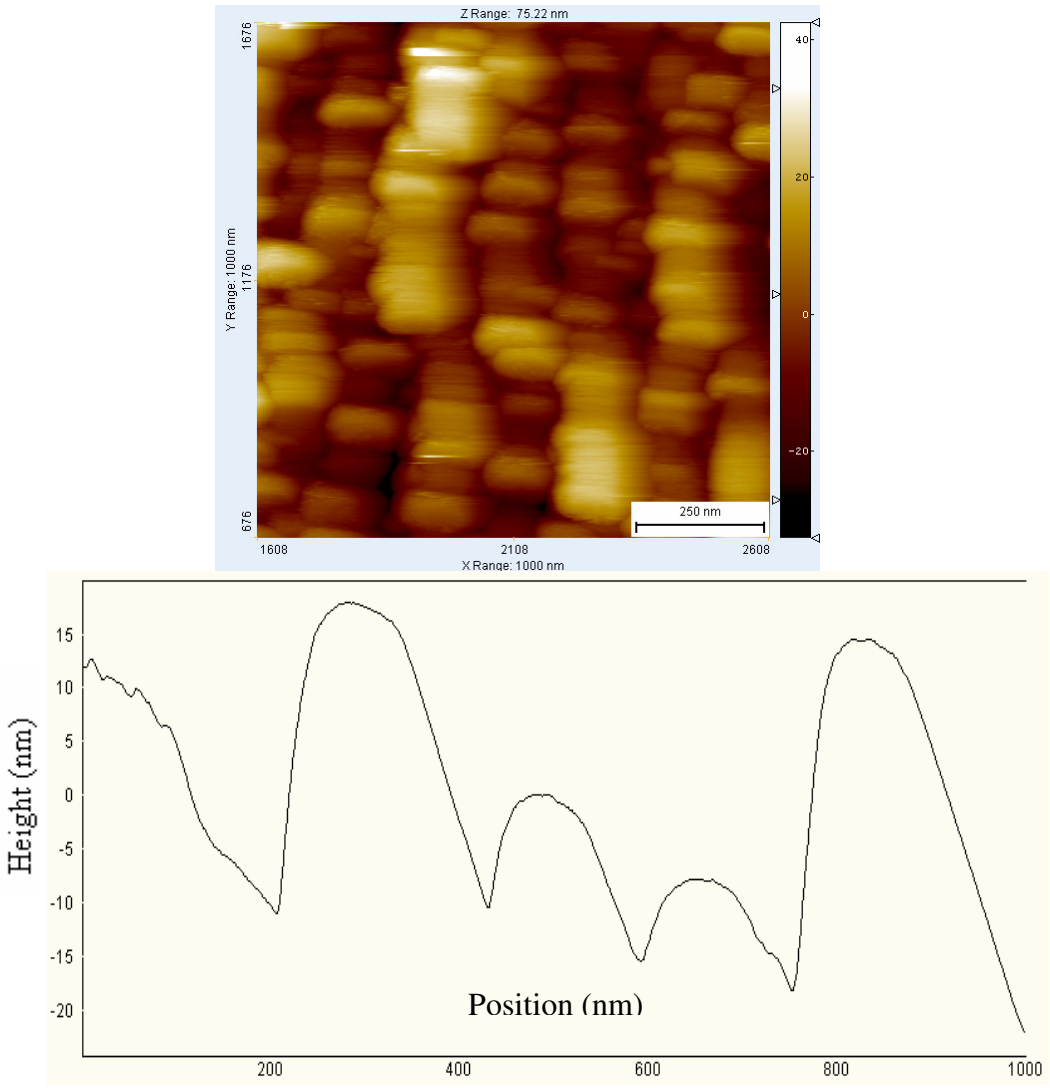


**Figure 4.6. STM image of 1 x 1 μm surface topography of InP (100) after $Ar^+$ ion bombardment at ion fluence of 5 x $10^{16}$ ions/cm$^2$ and its roughness profile at the center of the image showing rms roughness of 10.6 nm.**

In Figure 4.7, surface topography of InP (100) after irradiating at ion fluence of 1.06 x $10^{17}$ ions/cm$^2$ shows nanodots of 75 – 150 nm in diameter. Nanodots are joined and merged together in series, which are parallel to the direction of the incident ion beam. The RMS roughness and wavelength were measured as 14.7 nm, 226.45 nm respectively.

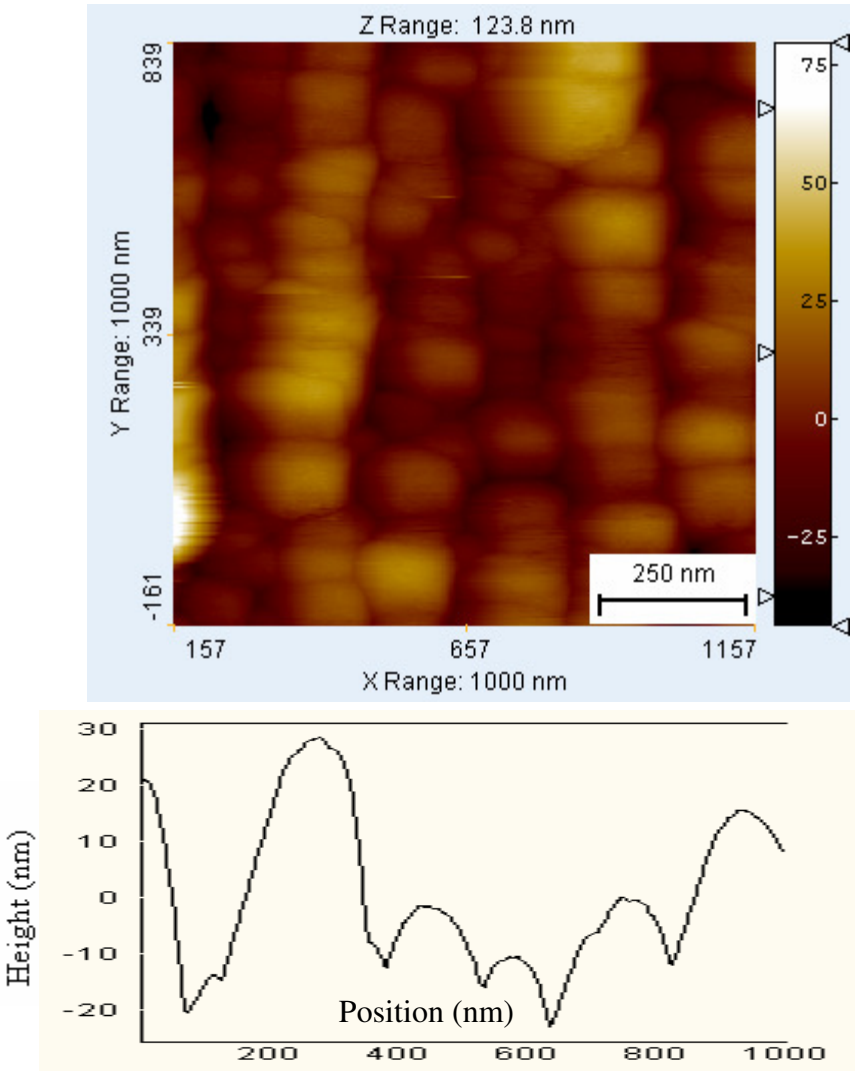


**Figure 4.7. STM image of 1 x 1 µm surface topography of InP (100) after $Ar^+$ ion bombardment at ion fluence of 1.06 x $10^{17}$ ions/cm$^2$ and its roughness profile at the center of the image showing rms roughness of 14.7 nm.**

In sequence, when fluence increased to 4.56 x $10^{17}$ ions/$cm^2$, it is very interesting that the series of nanodots totally disappeared and a completely new structure evolved. Figure 4.8, shows STM image of the InP (100) surface topography, which resembles a series of nanoflakes linked to a branch. Both the RMS roughness and the wavelength were measured from the average profile of the auto-correlated image and are 14.6 nm, 252 nm, respectively.

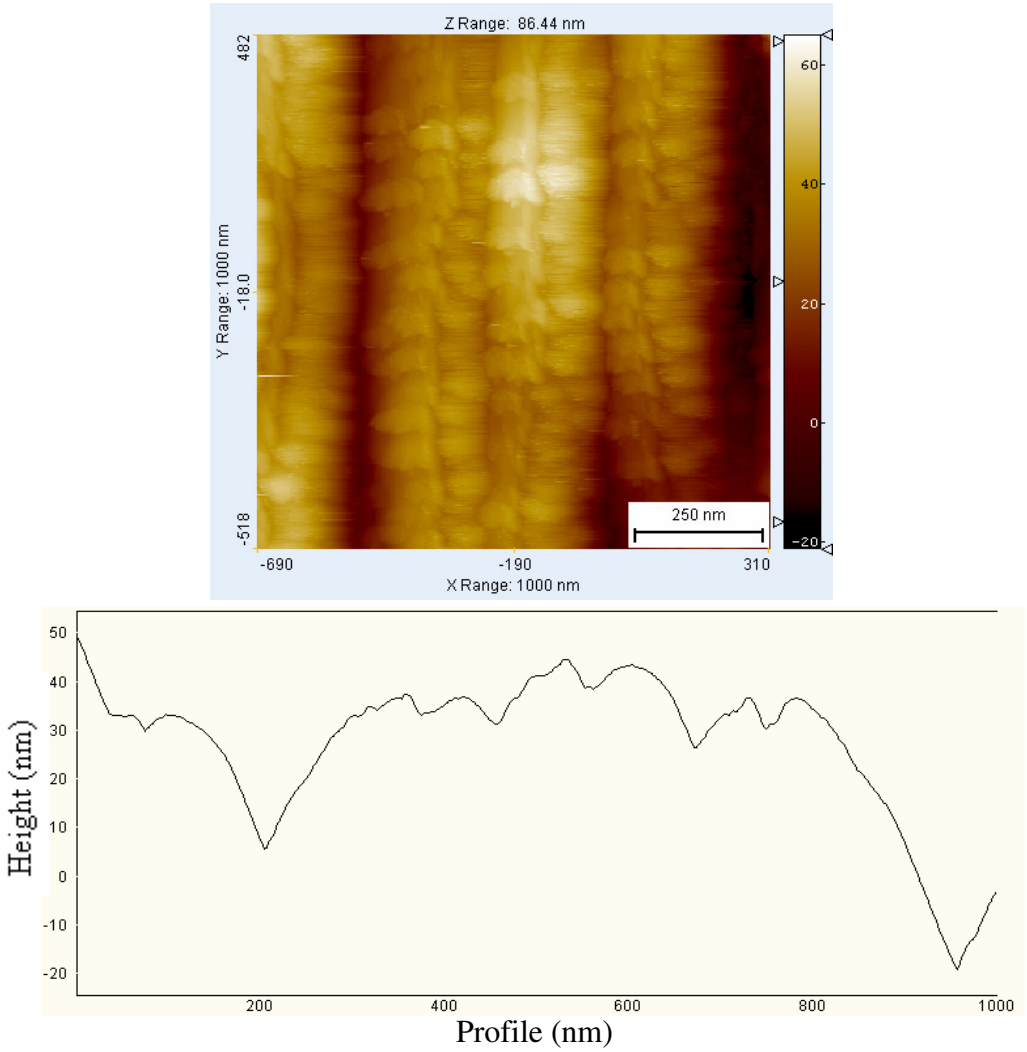


**Figure 4.8. STM image of 1 x 1 µm surface topography of InP (100) after $Ar^+$ ion bombardment at ion fluence of 4.56 x $10^{17}$ ions/$cm^2$ and its roughness profile at the center of the image showing rms roughness of 14.6 nm.**

### 4.3.1 Ion fluence dependence

The dependence of the ripple wavelength on the ion fluence is shown in Figure 4.9. Wavelength of the nanostructures increases with ion fluence and scales with the logarithm of the fluence (φ), which is not in agreement with Bradley and Harper theory predictions [3].

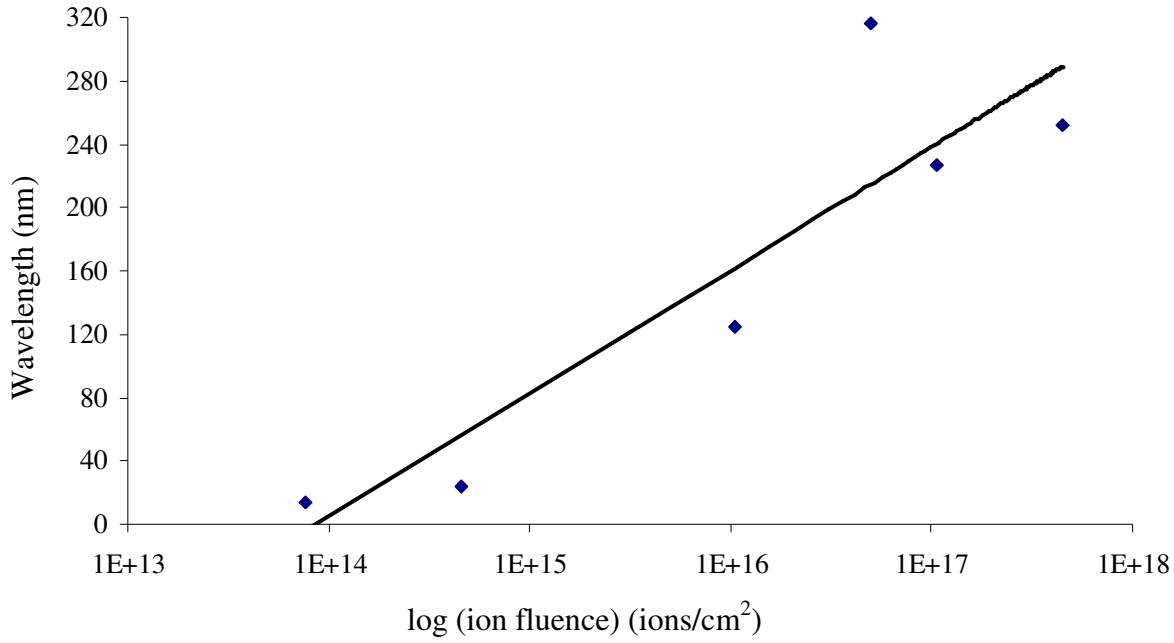


**Figure 4.9. Dependence of the ripple wavelength λ on the log of the ion fluence *Φ*.**

Figure 4.10, shows the dependence of the RMS roughness on the fluence. As the ion fluence increases, RMS roughness increased to $1x10^{17}$ ions/cm$^2$ and saturated as the fluence increased further. It indicates that the height of the nanostructures increased with fluence upto a limit and saturated beyond that limit. The increase in rms roughness is connected to the development of the sputtered nanodots and ripples.

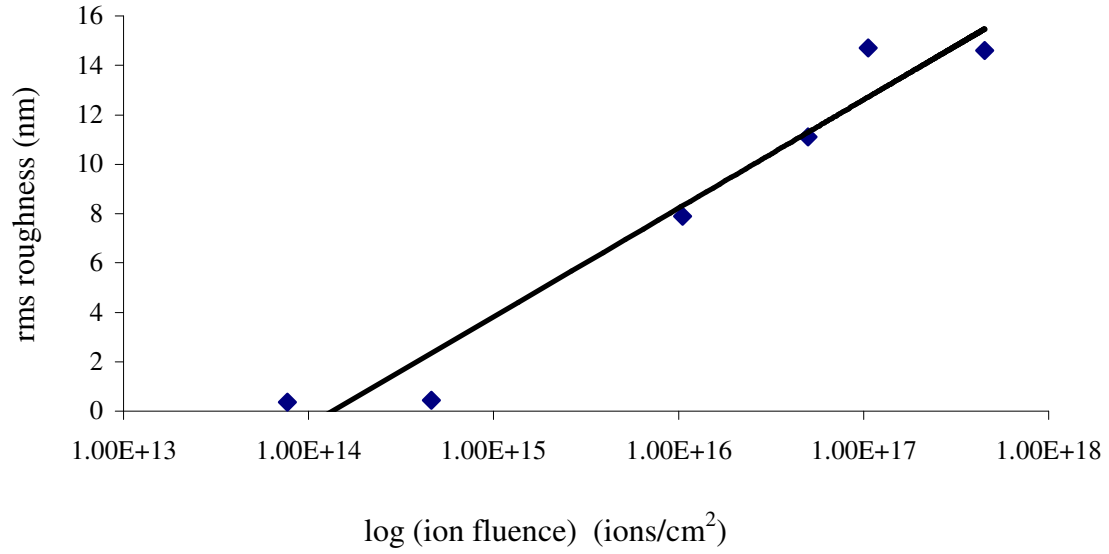


**Figure 4.10. Dependence of the rms roughness on log of the ion fluence *Φ*.**

Generally, any pattern formation on the ion-irradiated surface can be attributed to competition between surface roughening driven by a curvature-dependent local sputter rate and smoothing caused by minimization of the surface free energy. Bradley and Harper [3] analytical theory was used to explain ion bombardment – induced periodic structures. They considered only the case when the substrate is at high temperatures bombarded with ions at a low flux J. Under these conditions the wavelength λ of the ripples is given by:

$$\lambda(\theta, E) = 2\pi\sqrt{\frac{2NB}{JaY(\theta, E)\left|\Gamma_i(\theta)\right|}} \qquad (4.1),$$

where $Y$ = Sputter yield of the bombarding ions

$E$ = Incident ion energy

$\theta$ = Angle of incidence,

$a$ = average depth range of energy deposition,

$B$ = Surface diffusion parameter and

$\Gamma$ = Angular parameter.

From equation 4.1, it is clear that the wavelength depends only on the ion flux $J$, but not on the fluence φ. For low temperature and high fluxes, i.e. when significant redistribution of substrate atoms occurs due to ion beam mixing, it is shown that equation 4.1 must be modified in this case, and the ripple wavelength is independent of the flux $J$ and scales as [64]:

$$\lambda \sim \varphi^{0.5} \tag{4.2}$$

Most of the experimentally measured wavelengths show an increase with increasing fluence and are independent of the flux $J$. Therefore, these results do not agree with either predictions of the Bradley–Harper theory, i.e. equations 4.1 or 4.2. A similar result was obtained for 5 keV $Xe^+$ bombardment of InP. Demanet et. al. [65] found that the wavelength of the ripples also increased with increasing fluence. The various reported results for the fluence and flux dependences of the ripple wavelengths on silicon exhibit a significant variation [64]. Erlebacher et. al. [66] found that at elevated temperatures between 750 K and 900 K, at 0.75 keV and at 67.5°, $\lambda \sim J^{0.5}$ is in agreement with the Bradley – Harper theory at high temperatures, according to equation 1.1. However, the reported room temperature measurements by various authors [67] exhibit no flux

dependence as predicted by equation 4.1. The wavelength as a function of the fluence either remained constant with increasing fluence, or increased.

### 4.3.2 Dependence of RMS roughness on the ion fluence

The development of surface roughness by increasing fluence has been explained by Carter [65] in terms of the time rate equation:

$$\frac{\partial h}{\partial t} = -\frac{JY(\theta, E)}{N} \qquad (4.3),$$

where $h$ is the local height, $Y$ is the sputter yield as a function of the incidence angle θ of the ions with energy E and the atomic density N of the substrate. Superficially it seems as if equation 4.3 predicts a linear proportionality between $h$ and the RMS roughness. The angular dependence of the equation complicates a direct comparison with our experimental data. According to the Bradley–Harper theory, the amplitude h of the periodic structures due to ion bombardment depends exponentially on the sputter time t (and, thus, on the ion fluence):

$$h(t) = h_0 \, exp \, (r, t) \qquad (4.4).$$

It is clear that our experimental data shows that the RMS roughness depends linearly on the logarithm of the fluence, which does not agree with either the Bradley–Harper theory [3] or the Carter et. al. interpretation of equation 4.4. In order to explain the experimental results one must resort to an alternative model based in essence on the Carter model [68], which is based on sputter etching. The increase in RMS roughness is linked to the development of nanoripples and nanodots in InP. Apart from the initial

growth phase of these ripples and nanodots, one expects that ‘‘further’’ growth rate of the nanodots size (reflected by the RMS roughness of the surface) would be inhibited by erosion of the nanodots or ripples by sputtering. The amount of material removed by sputtering is directly proportional to the sputter time *t*, which is again directly proportional to the fluence $\varphi$. Therefore, it is expected that the erosion-inhibited growth rate of the sputtered nanodots and ripples would be given by:

$$\frac{dh_{rms}}{d\varphi} \alpha \frac{1}{\varphi} \tag{4.5}.$$

The solution of this Eq. (4.5) easily follows:

$$\varphi = \Phi e^{\gamma h}{}_{\mathrm{rms}} \tag{4.6}.$$

The growth parameter γ depends primarily on the bombardment species and varies due to the differences in the sputter yields. Equation 4.6 predicts that rms roughness is directly proportional to the logarithm of the fluence $\varphi$. The experimental data shown in Fig. 4.10 approximately follows this logarithmic dependence on the fluence $\varphi$.

### 4.3.3 Mechanical properties of InP before and after irradiation

Figure 4.11 shows the hardness and elastic modulus of the InP substrate before and after irradiation. Hardness of the irradiated InP is greater than fresh InP substrate for depths less than 20 nm and beyond that hardness is constant for both samples, which is attributed to the amorphisation of the surface after bombarding it with $Ar^+$ ions. Irradiated InP shows higher elastic modulus than the fresh InP substrate for depths less than 55 nm.

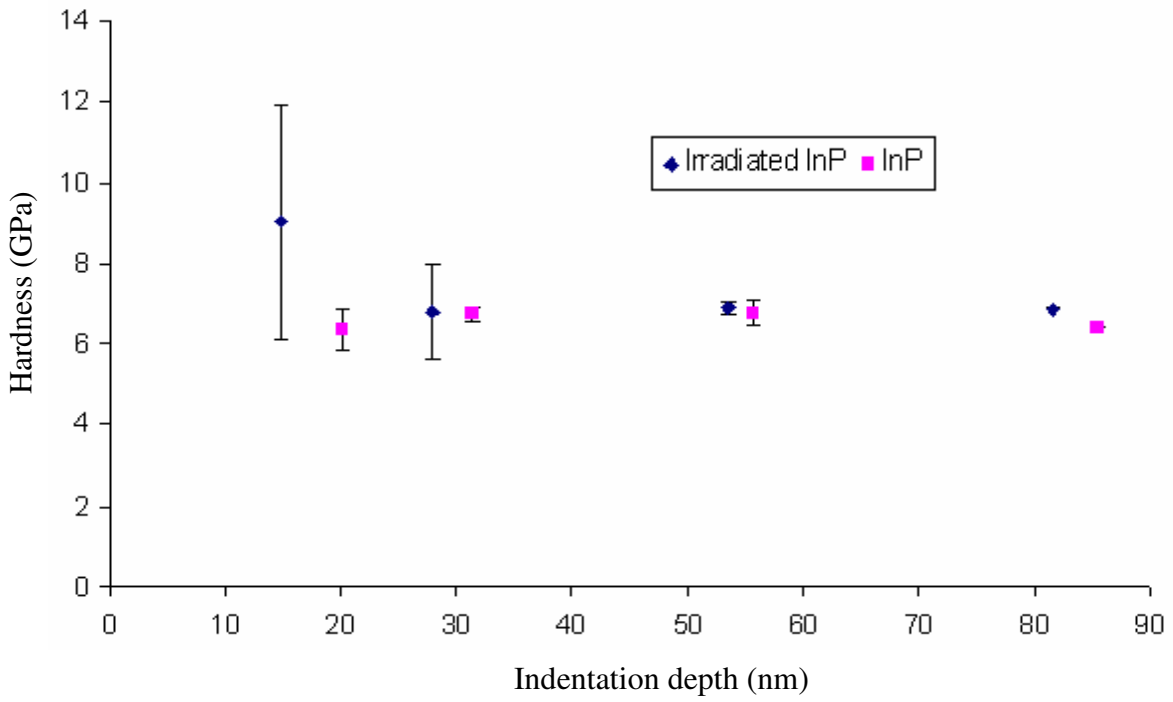


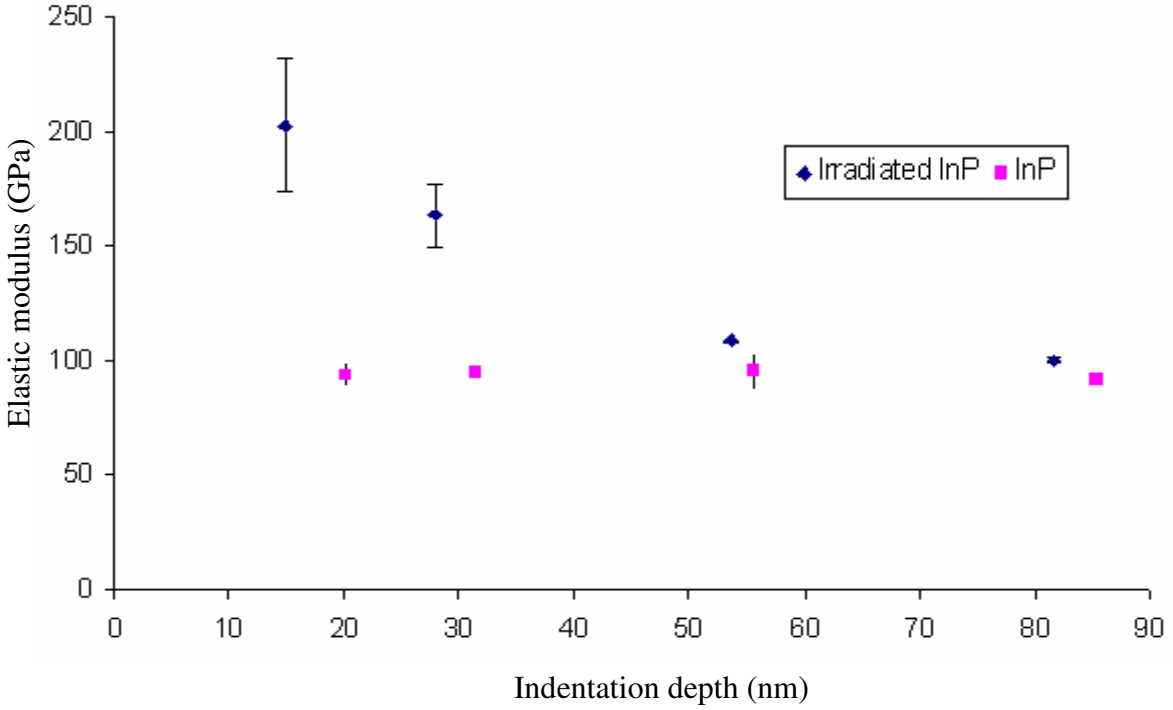


**Figure 4.11. Hardness and elastic modulus of InP (100) before and after $Ar^+$ ion bombardment.**

# Chapter 5

# Conclusions and Future Work

## 5.1 Conclusions

In this work, formation of nanowear ripples/nanostructures in two different materials using two different techniques has been studied. In first case, formation of tip-induced nanowear ripples was studied on the surface of single crystal calcite in the ambient environment using Hysitron Triboindenter. Ripple structures were observed at different contact loads and at different scanning frequencies by scanning the surface repeatedly with a Berkovich diamond tip. Secondly, nanostructuring of Indium Phosphide single crystal was studied after bombarding its surface with $Ar^+$ ions as a function of ion influence in the ultra high vacuum environment. Scanning tunneling microscopy was used to study the surface of InP single crystal after ion bombardment.

### 5.1.1 Tip-induced wear ripples on single crystal calcite

Formation of nanowear ripples was studied when a sharp diamond tip was scanned in contact with the calcite single crystal surface as a function of scanning speed and contact load of the tip. This phenomenon occurred through a complex interplay of experimental conditions and material properties. At 3 Hz frequency, wear ripples initiated at the first scan, and oriented perpendicular to the scan direction. Ripple structure initiation occurred at the bottom slope of the surface and

ripples propagated as number of scans increased. Once the ripples are fully developed on the surface, they started merging together increasing the height and periodicity with the number of scans. Ripple structure existed even after scanning the surface beyond 100 scan cycles. At 6 μN contact load, once ripple structure developed fully on the surface, the tip started removing the ripple structure as scanning continued further and wear occurred on the surface of the crystal. A completely fresh layer could be seen after few scan cycles at this load and no ripples appeared. As the load increased further (8 μN), the tip started removing the surface layer of the calcite crystals and the ripple structure did not initiate at all. At 1 Hz scanning frequency, tip-induced wear ripples were not initiated and the tip started removing the surface layer from the bottom of the sloped surface. As the scanning progressed further, the tip removed the top layer and a completely new surface was in contact with the tip. As the load increased at this frequency, similar behavior occurred, but a new surface appeared in less number of scan cycles.

### 5.1.2 Nanostructuring of InP (100) by ion bombardment

Production of nanostructures on the Indium Phosphide (100) surface has been studied during $Ar^+$ ion bombardment as a function of ion influence. In this work, InP (100) surfaces were irradiated at room temperature under ultra high vacuum (~$10^{-10}$ Torr) environment by 3 KeV $Ar^+$ ions at an incidence angle of $75^o$ to the sample normal. Nanostructures developed, and the surface topography have been studied as a function of ion influence using scanning tunneling microscopy. The evolved surface topographies were analyzed in terms of predictions of the Bradley – Harper theory. At lower fluences ($\Phi \leq 4.6 \times 10^{14}$ ion/cm$^2$), surface of InP developed nanoripples along the incident ion beam direction which were uniformly distributed on the surface, having a wavelength of

24 nm and rms roughness of 0.44 nm. As the fluence increased further ($\Phi$ = 1 x $10^{16}$ ions/$cm^2$), surface topography changed drastically and size of the nanostructures increased. At this fluence, surface topography of InP shows nanoripples of larger size ($\lambda$ = 125 nm and rms roughness = 8 nm) which are in the form of collection of nanodots oriented along the incident ion beam direction. As fluence increased further ($\varphi$ = 4.6 x $10^{17}$ ions/$cm^2$), surface topography shows interesting features and nanoripple structure was in a completely different form, shown in Figure 4.13. The rms roughness showed an approximate linear relationship with the logarithm of the fluence. Ripple wavelength linearly increased with ion fluence and wavelength of the nanostructures increased with ion fluence and scaled with the logarithm of the fluence ($\varphi$). Nanoindentation experiments were performed on the InP surface before and after ion bombardment to determine variations in hardness (H) and elastic modulus (E). It was found that irradiated InP showed higher H and E values at the surface as the surface became amorphized after $Ar^+$ ion bombardment.

## 5.2 Future work and recommendations

In this work, tip-induced nanowear ripples were observed on calcite single crystal in the ambient environment only. Variety of other materials (singe crystal or polycrystalline) can be tested with tips of different radii and at different orientations under various environments. The exact mechanism responsible for the formation of the tip-induced ripples is yet to be understood. One could model the scan process and system dynamics to determine the conditions at which surface ripples. So far tip-induced ripples were observed in KBr, Al and calcite single crystals using Hysitron Triboindenter in the ambient environment. We made an effort to create wear ripples on various

semiconductors (Si, GaAr, InSb, etc.), but did not observe ripple patterns at low 2 μN normal load, 3 Hz frequency, and 5 μm scan size. It could be worth to perform wear experiments at higher contact loads and at various scan sizes on these samples. In our experiments, Berkovich diamond tip was used to scan the surface of the calcite surface. Since it is a three-sided pyramidal tip and has 143.5° included angle, the wear process is complex, so it is difficult to predict the sample surface and tip interaction. One can conduct the wear experiments (repetitive scanning) with the conical tip (having tip radius in microns) at various scanning parameters. Wear behavior can be studied when the material surface is surrounded by water or other fluids. One can also conduct these experiments by purging nitrogen or noble gases to have better environmental control.

In this work, nanostructuring of InP by $Ar^+$ ion bombardment as a function of ion fluence at room temperature has been studied in UHV environment. Modification of the surface topography was evaluated using STM. Modifications of surface topography can be studied by varying different parameters such as ion flux, substrate temperature, incident ion energy and angle of incidence using different ion sources ($O^+$, $N^+$, $Ar^+$, etc).

References


1. M. Navez, C. Sella and D. Chaperot, *C.R. Acad. Sci., Paris* 254 (1962) 240

2. G. Carter, M. Nobes, F. Paton, J. Williams and J. Whitton, *Radiat. Eff.* 65 (1977) 33

3. R. Bradley and J. Harper, *J. Vac. Sci. Technol.* A 6 (1988) 2390

4. P. Sigmund, *J. Mater. Sci.* 8 (1965) 1545

5. G. Carter, *J. Phys. D: Appl. Phys.* 34 (2001)R1

6. T. M. Mayer, E. Chason and A. Howard, *J. Appl. Phys.* 76 (1994)1633

7. M. Szymonski, F. Krok, B. Such, P. Piatkowski, J.J. Kolodziej, "Ripple Creation on InSb (001) Surface Ions vs. AFM Tip", 3rd EFS Nanotribology Conference, Lisbon, Portugal, 18-22 September, 2004

8. R. Magno, and B.R. Bennett, *Appl. Phys. Lett.* 70 (1997) 1855

9. J. Cortes Rosa, M. Wendel, H. Lorenz, J.P. Kotthaus, M. Thomas, and H. Kroemer, *Appl. Phys. Lett.* 73 (1998) 2684

10. H.W. Schumacher, U.F. Keyser, U. Zeitler, R.J. Haug, and K. Eberl, *Appl. Phys. Lett.* 75 (1999) 1107

11. J. Regul, U.F. Keyser, M. Paesler, F. Holhs, U. Zeitler, R.J. Haug, A. Malave, E. Oesterschulze, D. Reuter, and A.D. Wieck, *Appl. Phys. Lett.* 81 (2002) 2023

12. C.M. Mate, G.M. McClelland, R. Erlandsson, and S. Chiang, Phys. Rev. Lett, 59 (1987)1942

13. E. Gnecco, R. Bennewitz, and E. Meyer, *Phys. Rev. Lett.* 88 (2002) 215501

14. A. Socoliuc, E. Gnecco, R. Bennewitz, and E. Meyer, *Phys. Rev. B* 68 (2003) 115416

15. T. Filleter, S. Maier, and. R. Bennewitz, *Phys. Rev. B* 73 (2006) 155433

16. O.M. Leung, and, M.C. Goh, *Science* 255 (1992) 64

17. Z. Elkaakour, J.P. Aime, T. Bouhacina, C. Odin, and T. Masuda, *Phys. Rev. Lett.* 73 (1994) 3231

18. X.P. Wang, M.M.T. Loy, and X. Xiao, *Nanotechnology,* 13 (2002) 478

19. B.D. Beake, P.H. Shipway, G.J. Leggett, *Wear,* 256 (2004) 118

20. M. Andersson, A. Iline, F. Steitz, F. Traeger, *Appl. Phys. A* 68 (1999) 609.

21. M. Pendergast, A.A. Volinsky, *Mat. Res. Soc. Proc*. 1021 E (2007) 110

22. Xiaolu Pang, Alex A. Volinsky, Kewei Gao, "Moisture Effects on Nanowear of Gold Films" submitted to Journal of Materials Research

23. G. Carter and V. Vishnyakov, *Phys. Rev. B* 54, 17 (1996) 647

24. J.J. Vajo, R.E. Doty, and E.H. Cirlin, *J. Vac. Sci. Technol. A* 14, (1996) 2709

25. Z. X. Jiang and P. F. A. Alkemade, *Appl. Phys. Lett.* 73, (1998) 315

26. E. Chason, T.M. Mayer, B.K. Kellerman, D.T. McIlroy, and A.J.Howard, *Phys. Rev. Lett.* 72, (1994) 3040

27. C.M. Demanet *et al., Surf. Interface Anal.* 23, (1995) 433

28. S. Rusponi, G. Costantini, C. Boragno, and U. Valbusa, *Phys. Rev. Lett.* 81, (1998) 4184

29. S. Rusponi, G. Costantini, C. Boragno, and U. Valbusa, *Phys. Rev. Lett.* 81, (1998) 2735

30. S. Facsko *et al.*, *Science* 285, 1551 (1999); B. Kahng *et al.*, Appl. Phys. Lett. 78, 805 (2001); M. Castro,R. Cuerno, L. Vazquez, and R. Gago, Phys. Rev. Lett. 94, (2005) 016102

31. S.W. MacLaren, J.E. Baker, N.L. Finnegan, and C.M. Loxton, *J. Vac. Sci. technol. A* 10, (1992) 468

32. G. Carter, *Surf. Interface Anal.* 25, (1997) 952

33. S. Facsko, T. Dekorsy, C. Koerdt, C. Trappe, H. Kurz, A. Vogt, H.L.Hartnagel, *Science* 285 (1999) 1551

34. S. Facsko, T. Bobek, H. Kurz, T. Dekorsy, S. Kyrsta, R. Cremer, *Appl. Phys. Lett.* 80 (2002) 130

35. F. Frost, A. Schindler, F. Bigl, *Phys. Rev. Lett.* 85 (2000) 4116

36. R. Gago, L. Vazquez, R. Cuerno, M. Varela, C. Ballesteros, J.M. Albella, *Appl. Phys. Lett.* 78 (2001) 3316

37. B. Ziberi, F. Frost, B. Rauschenbach, T. Hoche, *Appl. Phys. Lett.* 87 (2005) 033113

38. T.K. Chini, M.K. Sanyal, S.R. Bhattacharyya, *Phys. Rev. B* 66 (2002) 153404

39. T.K. Chini, D. Datta, S.R. Bhattacharyya, M.K. Sanyal, *Appl. Surf. Sci.* 182 (2001) 313

40. F. Krok, J.J. Kolodziej, B. Such, P. Piatkowski, M. Szymonski, *Appl. Surf. Sci*. 210 (2003) 112

41. F. Krok, J.J. Kolodziej, B. Such, P. Piatkowski, M. Szymonski, *opt. Appl.* XXXII (2002) 221

42. M.J. Nobes, G.W. Lewis, G. Carter, J.L. Whitton, *Nucl. Instr. And Meth*. B 170 (1980) 363

43. J.B. Malherbe, *Crit. Rev. Solid State Mater. Sci*. 19 (1994) 129

44. J.B. Malherbe, P. Chakraborty, "Ion Beam Analysis of Surfaces and Interfaces of Condensed Matter Systems", Nova Science, New York, 2003, p. 357 (Chapter 11)

45. P. Sigmund, *J. Mater. Sci.* 8, (1973) 1545

46. C. Herring, in: W. E. Kingston (Ed.), *physics of Powder Metallurgy*, McGraw-Hill, Newyork, 1951

47. W. W. Mullins, *J. Appl. Phys.* 30 (1959) 77

48. A. Datta, W. Yuh-Renn and Y.L. Wang, *Phys. Rev. B* 63 (2001) 125407

49. R. Gago, L. Vazquez, R. Cuerno, M. Varela, C. Ballesteros and J.M. Albella, *Appl. Phys. Lett.* 78 (2001) 3316

50. S. Park, B. Kahng, H. Jeong, A.L. Barabasi, *Phys. Rev. lett*. 83(1999) 3486

51. R. Cuerno, A.L. Barabasi, *Phys. Rev. lett.* 74 (1995) 4746

52. S. Rusponi, G. Costantini, C. Boragno, and U. Valbusa, *Phys. Rev. Lett.*81,(1998) 4184

53. Facsko S, Bobek T, Dekorsy T and Kurz H *Phys. Status Solidi* b 224 (2001) 537

54. Facsko S, Dekorsy T, Koerdt C, Trappe C, Kurz H, Vogt A and Hartnagel H L *Science* 285 (1999) 1551

55. D.A. Bonnell, "Scanning probe microscopy and spectroscopy: Theory, techniques, and applications", 2nd edition,

56. G. Binnig, H. Rohrer, *Phys. Rev. Lett.* 57 (1982) 49

57. G. Binning, C.E. Quate, Ch. Gerber, *Phys. Rev. Lett*. 56, (1986) 930

58. "Nanoindentation" 2nd edition, by Anthony C. Fisher – Cripps

59. W.C. Oliver and G.M. Pharr, J. Mater. Res., 74, (1992) 1564

60. "Triboindenter users manual" by Hysitron Inc., Minneapolis, MN (2003)

61. P. Zelinski, "Chatter control for the rest of us", Modern machine shop magazine, October 2005

62. E.P. Degarmo, J.T. Black, R.A. Kohser, "Materials and processing in manufacturing", John Wiley & sons, 9th ed., (2003) 504

63. J.B. Malherbe, J.M. Sanz, S. Hofmann, *Surf. Interface Anal*. 3 (1981) 235

64. J.D. Kiely, D.A. Bonnell, *J. Vac. Sci. Technol. B* 15 (4) (1997) 1483

65. J.B. Malherbe, P. Chakraborty (Ed.), Ion Beam Analysis of Surfaces and Interfaces of Condensed Matter Systems, Nova Science, New York, (2003) 357

66. C.M. Demanet, J.B. Malherbe, N.G. van der Berg, K.Vijaya Sankar, *Surf. Interface Anal.* 23 (1995) 433

67. J. Erlebacher, M.J. Aziz, E. Chason, M.B. Sinclair, J.A.Floro, *Phys. Rev. Lett*. 82 (1999) 2330

68. G. Carter, B. Navinsek, J.L. Whitton, in: R. Behrisch (Ed.), Sputtering by Particle Bombardment II, Springer-Verlag, Berlin, (1991) 231